1   Changes in Physical Properties of 4C Pyrrhotite (Fe$_7$S$_8$) across the 32 K Besnus Transition

2   Revision 1

3   Michael W. R. Volk[a*], Eric McCalla[b,c], Bryan Voigt[b], Michael Manno[b]

4   Chris Leighton[b], Joshua M. Feinberg[a]

5   [a] Institute for Rock Magnetism, Department of Earth Sciences, University of Minnesota,

6   116 Church Street SE, Minneapolis, MN 55455

7

8   [b] Department of Chemical Engineering and Materials Science, University of Minnesota,

9   421 Washington Ave. SE, Minneapolis, MN 55455

10

11   [c] Chemistry Department, McGill University, 801 Sherbrooke St. W, Montréal, Québec, Canada, H3A 0B8

12

13   Abstract

14   Pyrrhotite Fe$_7$S$_8$ is a common sulfide mineral in the Earth's crust and mantle, as well as in a

15   range of meteorites, and is of interest to a wide variety of disciplines, including economic geology,

16   geophysics, and material science. The 4C variety of pyrrhotite shows a dramatic change in

17   magnetic properties at $T \approx 30$ K, known as the Besnus transition. Although this transition is

18   frequently used to detect pyrrhotite in geologic samples, the underlying mechanism driving the

19   transition has not yet been identified. This study presents a high-resolution view of the changes in

20   heat capacity, magnetic, and electronic properties of a natural single crystal of nearly pure,

21   monoclinic 4C pyrrhotite across the Besnus transition. Contrary to previous studies, *all* of these

22   properties show clear evidence of the Besnus transition, specific heat in particular revealing a clear

23   transition at 32 K, apparently of second order nature. Small-angle neutron scattering data are also

24   presented, demonstrating an unusual change in short-range magnetic scattering at the transition.

*Corresponding author: Michael Volk, Institute for Rock Magnetism, Department of Earth

Sciences, University of Minnesota, 116 Church Street SE, Minneapolis, MN 55455x

*Email address:*mvolk@umn.edu (Michael W. R. Volk)

25 Furthermore, a magnetic field dependence of the transition temperature can be seen in both induced

26 magnetization and electrical resistivity. These new observations help narrow the possible nature

27 of the phase transition, clearly showing that interactions between intergrown coexisting 4C and

28 5C* superstructures, as suggested in some literature, are not necessary for the Besnus transition.

29 In fact, the changes seen here in both the specific heat and the electronic transport properties are

30 considerably larger than those seen in samples with intergrown superstructures. To further

31 constrain the mechanism underlying the Besnus transition, we identify five separate potential

32 models and evaluate them within the context of existing observations, thereby proposing

33 experimental approaches that may help resolve ongoing ambiguities.

34 Keywords: Besnus transition, Phase transition, magnetism, heat capacity, resistivity, Sulfide,

35 Pyrrhotite,

36 **1 INTRODUCTION**

37 Iron mono-sulfides, or pyrrhotites, ($Fe_{1-x}S$, $0 < x < 0.125$), are commonly occurring iron sulfide

38 minerals that are important to a wide range of scientific disciplines. In the Earth and planetary

39 sciences, 4C pyrrhotite (Fe_7S_8) acts as a recognizable ferrimagnetic phase, and is found in many

40 magmatic and metamorphic rocks (*Dunlop and Özdemir, 1997*), in claystones (*Aubourg and Pozzi,*

41 2010), and in limestones (*Muttoni,* 1995). In terrestrial rocks, the remanent magnetization carried

42 by this phase has been used to study polarity reversals of the Earth's magnetic field (e.g.,

43 *Quidelleur et al.,* 1992), to examine the nature of magnetization in quartzite clasts from the

44 Precambrian Jack Hills of Western Australia (*Weiss et al.*, 2015), and as the basis for a crustal geo-

45 thermometer (*Aubourg and Pozzi,* 2010) or barometer (*Gilder et al.,* 2011). Furthermore, 4C

46 pyrrhotite is a major magnetic constituent of several classes of meteorites, most notably in Martian

47 meteorites (*Rochette et al.,* 2001). Since pyrrhotite is thermodynamically stable on the surface of

Preprint submitted to American Mineralogist February 15, 2018

48   Mars, it may also contribute to the Martian magnetic anomalies (*Fegley Jr. et al., 1995*). Moreover,

49   4C pyrrhotite can be found in chondritic meteorites, the most primitive and oldest class of

50   meteorites (*Herndon et al.,* 1975, *Zhang et al.*, 2008), and, as such, may possibly record the

51   magnetic fields in the early solar system, as well as transient fields associated with impact events

52   (*Muxworthy et al.,* 2017). In general, pyrrhotites are also the most common iron sulfide minerals

53   in certain intrusions, such as the 1.1 Ga Duluth Complex, which hosts economically important

54   quantities of Cu, Ni and Pt group elements. Understanding the oxidation kinetics of pyrrhotite

55   minerals in mine tailings is of critical importance for avoiding water quality degradation due to

56   acid mine drainage (*Lapakko, 2015*). Further, pyrrhotite commonly occurs as inclusions in

57   diamonds, and may provide information about sulfur cycling within the lower mantle (*Sharp,*

58   *1966, Gilder et al. 2011*). Within the material science community, pyrrhotites have been studied

59   as potential candidate materials for anodes in lithium-ion batteries (*Zhang et al.,* 2015), and can

60   be used to sequester arsenic contamination in the environment (*Cantu et al.,* 2016).

61   Given its importance to geoscience and material science, proper characterization of pyrrhotite

62   within natural and synthetic samples is critical, yet frustratingly difficult. As discussed in more

63   detail below, iron monosulfides can display a wide range of crystallographic symmetries and

64   superstructures based on their composition and growth history, and frequently occur as finely

65   intergrown polycrystalline assemblages. Thus, reflected light and electron microscopy methods

66   are often combined with electron and neutron diffraction to properly determine the structure of

67   small iron monosulfide grains. However, magnetic methods are one of the few techniques that

68   allow researchers to characterize the presence of pyrrhotite in bulk samples. In particular,

69   observations of the low-temperature magnetic transition at approximately 30 K (the "Besnus"

70   transition) of 4C pyrrhotite have been used with increasing frequency as a diagnostic indicator for

3

71   the presence of pyrrhotite (*Dunlop and Özdemir, 1997*). Low temperature superconducting

72   quantum interference device (SQUID) magnetometers are typically sensitive enough to detect 4C

73   pyrrhotite in natural samples at parts per million concentrations (*Rochette et al.* 1990).

74   Despite the utility of low temperature magnetic methods in detecting the presence of pyrrhotite

75   in natural and synthetic samples, there is remarkably little consensus on the mechanism that

76   underlies this dramatic change in magnetic properties. The aim of this study is to provide a high-

77   resolution view of the physical (heat capacity and resistivity) and magnetic properties (remanence

78   and high- and low-field induced magnetization) across the Besnus transition in a phase-pure

79   specimen of 4C pyrrhotite. Small angle neutron scattering is also presented to help determine the

80   length scales over which the changes in magnetic properties take place. This new data provides

81   the necessary evidence to differentiate between competing models that seek to explain this

82   phenomenon, and will enable researchers to more accurately interpret its magnetic recording on

83   Earth and other planetary bodies.

84   **1.1   SUPERSTRUCTURES**

85   Pyrrhotite occurs in many polytypes that are often intergrown or show incommensurate

86   chemical composition. Similar to troilite (FeS), these polytypes crystallize in a NiAs-like structure

87   with alternating filled and vacant Fe layers oriented parallel to the *ab* plane containing variably

88   ordered vacancies (*Morimoto et al.,* 1970). Within each Fe-layer the spins are coupled

89   ferromagnetically. However, adjacent layers are coupled antiferromagnetically via superexchange

90   through the S atoms, which in turn forms distorted S octahedra around the Fe atoms (*Levinson and*

91   *Treves*, 1968). Ordering of the vacancies gives rise to superstructures, which are referred to using

92   an *NC* notation, where *N* gives the number of stacked NiAs cells along the crystallographic *c*-axis.

93   Four commensurate hexagonal varieties, FeS (2C), Fe_9S_{10} (5C), $Fe_{10}S_{11}$ (11C) and $Fe_{11}S_{12}$ (6C),

4

94   and one monoclinic Fe_7S_8 (4C) are stable at ambient conditions (*Nakazawa and Morimoto*, 1970;

95   *Morimoto et al.*, 1970). The ordering of the vacancies in hexagonal polytypes creates a zero net

96   magnetization, and thus hexagonal pyrrhotites are non-ferro/ferri-magnetic in the bulk, and

97   incapable of retaining a spontaneous magnetization.

98   On the other hand, ordering of vacancies in the most Fe deficient variety of pyrrhotite, Fe_7S_8

99   (4C), creates a small lattice distortion ($\beta \neq 90$), which lowers the mineral's symmetry to monoclinic

100   (*Powell et al. 2004*), and is often referred to as 'pseudo-hexagonal'. Furthermore, the ordered

101   vacancies in 4C pyrrhotite produce a small net magnetization, which gives rise to ferrimagnetism

102   up to its Néel temperature of 598 K *(Powell et al., 2004)*. Within the 4C cell, the layers can be

103   labeled as *FAFBFCFD*, where F denotes a filled Fe layer and A-D are four distinct vacancy layers.

104   Each layer with vacancies contains four unique Fe sites (*Bertaut*, 1953; *Tokonami et al.*, 1972). Of

105   these Fe sites, two have no vacancies above or below, while the Fe atoms in the filled (F) layers

106   are adjacent to either one or two vacancies (*Ericsson et al.*, 1994). Superexchange coupling

107   through the S atoms is stronger than the direct Fe-Fe coupling (*Levinson and Treves*, 1968).

108   Consequently, sites that do not have vacancies above or below should be largely unaffected by

109   changes in vacancy ordering (*Levinson and Treves*, 1968).

110   **1.2 PHASE TRANSITION**

111   At $T_{Bes} \approx 30$ K, 4C pyrrhotite undergoes a magnetic phase transition first described by *Besnus*

112   *and Meyer* (1964). The Besnus transition is commonly used to identify pyrrhotite in rocks

113   (*Rochette et al.*, 2011). Similar to the Morin transition in hematite (Fe_2O_3) or the Verwey transition

114   in magnetite (Fe_3O_4), the transition is marked by a loss of remanent magnetization on cooling, and

115   a drastic change in fundamental magnetic properties (*Fillion and Rochette*, 1988; *Dekkers et al.*,

116   1989; *Rochette et al.*, 1990, Dunlop and Özdemir, 1997). Furthermore, the anisotropy constants

117   and the direction of the magnetic easy axis change during cooling (*Mikami et al.*, 1959; *Bin and*

118   *Pauthenet*, 1963; *Sato et al.*, 1964; *Rochette et al.*, 1990). At room temperature (T_R) the easy axis

119   lies within the basal (*a-b*) plane of the crystal but this progressively rotates out of the basal plane

120   towards the *c* axis upon cooling below 205 K (*Bin and Pauthenet*, 1963, Powell et al. 2004). While

121   a self-reversal of the magnetization has been observed in very large pyrrhotite crystals (*Fillion and*

122   *Rochette*, 1988), the direction of the remanence vector at room temperature, remains constant upon

123   cycling through T_{Bes} (*Feinberg et al.*, 2015).

124   While the Besnus transition has been known to our community for more than 50 years, the

125   mechanism driving the transition is not well understood. Two prevailing explanations exist.

126   *Wolfers et al.* (2011) measured neutron diffraction and magnetic torque on twinned single crystals.

127   The magnetic torque shows a six-fold symmetry above T_{Bes}, which changes to a four-fold

128   symmetry below the transition. Based on the change in symmetry, *Wolfers et al.* (2011) propose a

129   crystallographic transition from the monoclinic $F2/d$ ($T > T_{Bes}$) to a triclinic F-1 ($T < T_{Bes}$) structure.

130   This mechanism is similar to the change from cubic to monoclinic symmetry that occurs within

131   magnetite upon cooling through the Verwey transition at $T \approx 110$ K. The second explanation was

132   proposed by *Charilaou et al.* (2015) and later expanded upon by *Koulialias et al.* (2016, 2018).

133   Here, the change in magnetic properties is explained by changing magnetic interactions between

134   two different coexisting superstructures (4C and 5C*). The proposed 5C* phase in *Charilaou et*

135   *al.* (2015) possesses a different vacancy ordering, but the same overall chemical composition as

136   the 4C structure. Their arguments against a crystallographic phase transition as the basis of the

137   Besnus transition are based in large part on the absence of a transition in the heat capacity $C_p(T)$,

138   and the presence of a second inflection in hysteresis loops at low temperatures ($T < 200$ K). Clearly,

139   this explanation relies on the existence of two distinct coexisting phases of $Fe_{1-x}S$.

6

140   In a previous study, we measured major hysteresis loops in 72 directions within the basal plane

141   of an oriented single crystal of phase-pure 4C pyrrhotite (*Volk et al.*, 2016). The chemical

142   composition and crystallographic orientation of the crystal were determined by Energy-dispersive

143   X-ray spectroscopy (EDX) and Electron backscatter diffraction (EBSD). The experiments were

144   conducted at 21 temperatures spanning the Besnus transition (20-50 K). Several magnetic

145   properties showed a six-fold symmetry above T_{Bes}, including the second hysteresis inflection

146   described by Koulialias *et al.* (2016). However, we found that these magnetic symmetries change

147   from six-fold ($T > T_{Bes}$) to four-fold ($T < T_{Bes}$), consistent with the behavior originally observed

148   by *Wolfers et al.*, (*2011*). Furthermore, the second hysteresis inflection disappeared below T_{Bes}. To

149   better differentiate between the competing models, we present here a detailed study of the

150   structural, magnetic and electronic properties of a second Fe_7S_8 single crystal subsampled from

151   the same piece used in Volk *et al.* (2016) from Morro Velho, Brazil, provided by the Munich

152   Mineralogical State Collection (Mineralogische Staatssammlung München).

153   **2   RESULTS AND DISCUSSION**

154   The chemical composition of the sample was determined by electron microprobe analysis with

155   a JEOL JXA-8900R operated with a beam energy of 20 keV, a current of 20 nA and diameter of

156   5 micron. Detection limits ranged from 0.020 weight percent for Fe Kα to 0.022 weight percent

157   for S Kα and analytical sensitivity (at the 99% confidence level) ranged from 0.157 percent relative

158   for Fe Kα to 0.406 percent relative for S Kα. Elements were acquired using analyzing crystals

159   LiFH for Fe-kα, and PETJ for S-kα. The standards were Fe for Fe Kα, and Pyrite, FeS_2 for S Kα.

160   The specimen's bulk chemical composition, determined from 12 measurements, is $Fe_{6.78\pm0.12}S_8$

161   ($Fe_{0.85}S$, Fe = 45.9 at. %). According to the phase diagram of *Nakazawa and Morimoto* (1971), the

162   sample's measured composition is within in the stability field of 4C pyrrhotite. Significantly, no

7

163 impurities, such as Ni, were detected in any of the 12 measurements (within the limits stated

164 above).

165 In naturally occurring rocks, pyrrhotites are often an intergrown mixture of both the hexagonal

166 and monoclinic phases (*Arnold*, 1967). In our case, it is particularly important to detect the

167 presence of any such hexagonal intergrowths, since one of the proposed mechanisms for the

168 Besnus transition requires the presence of both 4C and 5C* superstructures (*Charilaou et al.*, 2015;

169 *Koulialias et al.*, 2016). Non-magnetic hexagonal phases transform into a ferrimagnetic

170 phasebetween 200°C-265°C depending on their iron content (Schwarz and Vaughan, 1972). This

171 transformation, due to a rearrangement of vacancies, is identified as a sudden rise in magnetic

172 susceptibility, known as the λ-transition (*Schwarz and Vaughan*, 1972). We measured magnetic

173 susceptibility as a function of temperature using a Geophysica Kappabridge KLY-2 (300 Am^{-1}

174 field at 920 Hz), which is able to detect even small hexagonal impurities. The specimen shows a

175 single Néel temperature (318°C, 591 K) close to the literature value (320°C (*Dunlop and Özdemir,*

176 1997)) with no sign of a lambda transition, as shown in Figure S1. This conclusion of the absence

177 of any significant amount of 5C* phase is supported by structure determinations, also, as discussed

178 below.

2.1 POWDER X-RAY DIFFRACTION

180 To detect possible inclusions (*e.g.,* pyrite FeS$_2$) in our pyrrhotite sample, or pyrrhotite

181 polytypes (*e.g.,* the 5C* phase discussed above), room temperature powder X-ray diffraction

182 (PXRD) data were acquired with a PANalytical X'Pert PRO X-ray diffractometer equipped with

183 a Co source (0.17909 nm) and an X'Celerator detector. The diffraction patterns were collected

184 from 10°-90° scattering angle in 0.0167° steps with an effective dwell time of 100 s per step.

8

Preprint submitted to American Mineralogist February 15, 2018

185   Figure 1 shows the PXRD pattern along with the result of Rietveld refinement with a single

186   phase with a 4C stacking sequence. The software Rietica was used to fit the data using the

187   structural model by *Powell et al.* (2004). The fitted cell parameters of the monoclinic space group

188     $C2/c$ are $a = 1.1915(1)$ nm$,$ $b = 0.68698(6)$ nm$,$ $c = 1.2907(1)$ nm and $\beta = 118.005(1)°$, with quality

189   parameters of $R_{bragg} = 2.87$ %$,$ $R_P = 2.24$ % and $R_{WP} = 3.51$ %. The lattice parameters agree well

190   with the values for the 4C phase obtained by *Charilaou et al.* (*2015*). Furthermore, the composition

191   obtained by PXRD refinement is $Fe_{6.76}S_8$ ($Fe_{0.83}S$), in excellent agreement with the measured

192   chemical composition from electron microprobe analysis. The PXRD results thus indicate that the

193   crystal is pure monoclinic 4C pyrrhotite without any detectable contamination from other minerals

194   (e.g., oxides) or vacancy superstructures. It is important to note that the hexagonal (5C*) phase,

195   which is clearly present in the PXRD data presented by *Charilaou et al.* (*2015*) (see Fig. 1 inset),

196   is not present here, within the limits of detection.

197   **2.2   SMALL ANGLE NEUTRON SCATTERING**

198   Small-angle neutron scattering (SANS) from a 4C pyrrhotite single crystal was used to

199   investigate potential structural and/or magnetic changes across the Besnus transition. This

200   powerful method (*Muhlbauer et al., 2018*), which has not yet been applied to pyrrhotite, provides

201   length-scale-dependent information on structural and magnetic inhomogeneities across a wide

202   range. In essence, the neutron scattering cross-section, $d\Sigma/d\Omega$, is measured as a function of the

203   scattering wavevector, Q, revealing information on a length scale $2\pi/Q$. Importantly, in the

204   unpolarized case used here, the inhomogeneities that generate the scattering can be structural (e.g.,

205   long-range defects, twins, twin boundaries) or magnetic (e.g., domains and domain walls, short-

206   range magnetic fluctuations, etc.). The SANS measurements presented were taken on the NG7 30

207   m SANS beamline at the NIST Center for Neutron Research, at 6 temperatures between 5 and 60

9

208   K, i.e., around the Besnus transition. At each temperature, 2D area scans, or Q_x-Q_y intensity maps

209   (see Fig. 2a), were collected in two frames (one at 0.004 Å^{-1} < Q < 0.025 Å^{-1} and one at 0.02 Å^{-1}

210   < Q < 0.15 Å^{-1}), resulting in a total covered Q range from 0.004 to 0.15 Å^{-1}. We thus probe real-

211   space length scales ($2\pi/Q$) from 4 to 160 nm. In such scans the neutron beam is perpendicular to

212   the plane of the detector, the dark region in the center of Fig. 2a is a beam-stop covering the

213   unscattered beam, and displacement outwards from the origin corresponds to increasing Q.

214   Fig. 2 shows the SANS results obtained with a sister specimen to the main crystal studied in

215   this work, oriented with the c-axis approximately parallel to the neutron beam. Panel (a) shows an

216   example 2D area scan (i.e., a Q_x-Q_y intensity map), at 5 K, out to Q_x/Q_y values of 0.02 Å^{-1}, i.e.,

217   probing real space length scales above 30 nm. The six-fold in-plane symmetry is obvious in the

218   2D scan, and, due to the use of unpolarized neutrons, could arise from structural effects (such as

219   long-range (> 30 nm) defects aligned with high-symmetry in-plane directions) or from magnetic

220   domain formation along specific axes (note that the data were recorded here after nominal zero

221   field cooling). Of high interest in terms of the aforementioned potential explanations for the Besnus

222   transition, the observed six-fold pattern *did not* alter significantly across the 32 K transition

223   temperature. The angular scan in Fig. 2b, which simply shows the cross-section summed over the

224   small range 0.005 Å^{-1} < Q < 0.009 Å^{-1} (to improve statistics), was in fact averaged over all

225   temperatures between 5 and 60 K, no significant changes in the angular dependence occurring at

226   any T. Six-fold periodicity is thus clear, but, remarkably, it is not T-dependent across the Besnus

227   transition. If a crystal symmetry change occurs at 32 K, this indicates that the long-range (> 30

228   nm) structural defects or magnetic domains producing the scattering seen here do not change

229   significantly in response.

10

230   There are, however, some subtle changes in the absolute scattering intensity. To illustrate this,

231   Fig. 2c plots $d\Sigma/d\Omega$ *vs.* the magnitude of Q, acquired by circular averaging of 2D maps of the type

232   shown in Fig. 2(a); the example shown here is at 45 K. As is often the case, $d\Sigma/d\Omega(Q)$ can be fit

233   (solid line through the points) as the sum of two terms: A Porod term (blue dashed line) and a

234   Lorentzian term (red dashed line). The generalized Porod term has the form $d\Sigma/d\Omega = (d\Sigma/d\Omega)_P/Q^n$,

235   where the exponent n provides details on the morphology of the scattering inhomogeneities, and

236   the prefactor $(d\Sigma/d\Omega)_P$ parameterizes the strength of the Porod intensity. In our case $n = 3.3$ (i.e.,

237   somewhat less than 4), as shown in Fig. 2c, indicating that the scattering inhomogeneities (long-

238   range structural defects or magnetic domains) do not have completely smooth surfaces. A value of

239   3.3, however, not far from the generic 4.0 for smooth 3D objects, indicates that the scattering is

240   *not* occurring from clearly one- or two-dimensional objects, such as filaments or lamellae. The

241   Lorentzian term has the form $d\Sigma/d\Omega = (d\Sigma/d\Omega)_L /(Q^2 + \kappa^2)$, where the prefactor $(d\Sigma/d\Omega)_L$

242   parameterizes the strength of the Lorentzian intensity, and κ is a constant. Such scattering is most

243   commonly associated with short-range (nm-scale) magnetic fluctuations, where κ becomes $1/\xi$,

244   the magnetic correlation length. Standard behavior in a ferrimagnet would involve an order-

245   parameter-like turn on of the Porod scattering from magnetic domains below the magnetic ordering

246   temperature, along with a peak in Lorentzian scattering at the ordering temperature due to critical

247   scattering. At $T \leq 60$ K, far below the ordering temperature, Lorentzian scattering should thus be

248   small, and, if present at all, be decreasing on cooling. Not only does Fig. 2c show that the

249   Lorentzian scattering here is non-negligible, but Fig. 2d shows that it has an unusual T dependence.

250   Specifically, $(d\Sigma/d\Omega)_L$ (right axis, red points) decreases on cooling from 60 to 35 K, as might be

251   expected, but then *grows* on further cooling to 5 K. This is unusual in a long-range-ordered ferro-

252   or ferri-magnet far below its ordering temperature. The Besnus transition thus manifests itself in

11

253   some change in short-range (< 10 nm) spin fluctuations/ordering in 4C pyrrhotite, but not

254   obviously so in the angular dependence of long-range (> 30 nm) scattering. We note that the T

255   dependence of $(d\Sigma/d\Omega)_P$ (left axis, black points in Fig. 2d) may provide some evidence of a plateau

256   around the Besnus transition, although much better statistics would be required to reinforce this.

257   Future SANS measurements to probe these findings in more detail could employ a much wider T

258   range (going above the Néel temperature), or polarized neutrons, to better separate magnetic and

259   structural scattering. Both of these approaches are certainly possible.

260   **2.3   HEAT CAPACITY**

261   As discussed above in the Introduction, the existence of an anomaly in specific heat capacity

262   (C_P) at the Besnus transition is important in pyrrhotite, but is not clear from prior experimental

263   work. Specifically, the work of *Grønvold et al.* (1959) indicated a small anomaly around 32 K,

264   while the work on material with mixed 4C/5C* superstructures by *Charilaou et al.* (2015) revealed

265   no such anomaly. In general, first-order phase transitions involve latent heat and result in

266   discontinuities in $C_P(T)$, while second-order transitions involve no latent heat and result in peaks

267   in $C_P(T)$. To probe these issues in our 4C pyrrhotite single crystal, $C_P(T)$ was measured in a

268   Physical Property Measurement System (PPMS) from Quantum Design Inc., from 1.8 K to room

269   temperature. Relaxation calorimetry was employed, using temperature pulses amounting to 2 % of

270   the sample temperature. The crystal was attached to the measurement platform using Apiezon N

271   grease, and the heat capacity of the platform and grease were subsequently subtracted. For all

272   measurements the ratio of sample to addenda heat capacity was maintained at greater than 2.0,

273   safely above the recommended minimum of 0.5 from *Lashley et al.* (2003). Similarly, the thermal

274   coupling parameter between the sample and calorimeter was > 96%, well above the minimum

275   Quantum Design recommendation of 90%.

276   Fig. 3 shows our $C_P(T)$ results along with those obtained from *Grønvold et al.* (1959),

277   *Kobayashi et al.* (1999), and *Charilaou et al.* (2015). Fig. 3a shows $C_P(T)$ over the entire T range

278   studied (1.8 - 300 K), *generally* showing good agreement with previous studies over most of the T

279   range. Around the Besnus transition, however (inset to Fig. 3a), the results are substantially

280   different in the various studies. In our work, $C_P(T)$ exhibits a large anomaly at 31.7 K, larger than

281   the one seen by *Grønvold et al.* (1959) (in a synthetic sample), and in contrast to the lack of any

282   anomaly seen by *Charilaou et al.* (2015). In the latter work, multiple stacking sequences (i.e.,

283   coexisting 4C and 5C* phases) were clearly observed in XRD. Here, however, we have a phase-

284   pure 4C pyrrhotite crystal, which apparently results in a clear, well-defined transition in $C_P(T)$,

285   taking the form of a classic "λ anomaly" expected at a second-order phase transition. (Note that

286   this is not to be confused with the 220 °C "λ-transition" in hexagonal pyrrhotite, as discussed

287   above). The apparent second-order nature of the transition is supported by the absence of any

288   detectable thermal hysteresis, both in relaxation calorimetry on cooling and warming, and by the

289   use of long-pulse measurements (*Gillard et al.* 2015). The striking differences between our phase-

290   pure 4C natural single crystal and the 4C/5C* natural crystal of *Charilaou et al.* (2015), may well

291   result from the phase-purity with respect to the stacking sequences, and/or trace concentrations of

292   other metals (particularly nickel). It is interesting to note that the 5C polymorph measured later by

293   *Grønvold et al.* (1991) (not shown in Fig. 3) also shows no $C_P(T)$ anomaly, suggesting that the

294   pure 4C structure may be the only form of pyrrhotite that displays a heat capacity anomaly at the

295   Besnus transition, and that any changes in properties across the Besnus transition are intrinsic to

296   4C pyrrhotite.

297   Subtracting a linear T-dependent background from our $C_P(T)$ data around the Besnus transition

298   and then integrating the excess specific heat yields the entropy change across the Besnus transition.

13

299   This gives 2.39 J mol^{-1} K^{-1}, or, by mole of Fe, 0.34 J mol^{-1} K^{-1}. For comparison, the entropy

300   change across the Verwey transition of magnetite, a first-order structural transition, is

301   approximately 5 J mol^{-1} K^{-1}, or by mole of Fe, 1.33 J mol^{-1} K^{-1} (*Shepherd et al.* 1991). Furthermore,

302   the Morin transition of hematite, a first-order spin-flop transition, has an entropy change of 0.43 J

303   mol^{-1} K^{-1}, or, per mole of Fe, 0.22 J mol^{-1} K^{-1} (*Pastor et al.* 2012). The entropy change across the

304   Besnus transition in 4C pyrrhotite is thus significant.

305   Further analysis was performed on the low T specific heat (Fig. 3b), which can be used to

306   extract electronic and lattice contributions, in turn allowing for determination of the density-of-

307   states at the Fermi level and the Debye temperature, respectively. (As discussed later in this work,

308   pyrrhotite is an electronic conductor). As shown in Fig. 3b, our $C_P(T)$ in this region is in excellent

309   agreement with that of *Kobayashi et al.* (1999), but again rather different to the mixed phase

310   4C/5C* crystal of *Charilaou et al.* (2015). Our data were fit following the standard procedure,

311   using $C_P(T) = \gamma T + \beta T^3 + \alpha T^5,$ where the first term is the electronic contribution and the latter two

312   are from lattice dynamics. The T^3 term is the standard low-temperature expansion in the Debye

313   model, while the T^5 term is the next order term, as often needed to adequately describe

314   experimental data. Two fitting procedures were employed, the first considering all data up to 10

315   K, comparable to that used by *Kobayashi et al.* (1999). This resulted in a poor fit, with an

316   unphysically large αT^5 term. The second fitting approach acknowledges the clear upturn in the data

317   at $T^2 < 30$ K^2, and fits only at $T^2 > 30$ K^2, resulting in the good fit shown in Fig. 3b. Considering

318   the electronic contribution first, the results give γ = 95 mJ mol^{-1} K^{-2}, a substantial value.

319   Theoretical values from the density-of-states at the Fermi level calculated from density functional

320   theory suggest ~46.5 mJ mol^{-1} K^{-2}, however (*Shirai et al.*,1996; *Shimada, et al.,* 1998),

321   corresponding to only a modest effective mass enhancement of ~2, in good agreement with

14

322   *Shimada et al.* (1998) and *Kobayashi et al.* (1999). With respect to lattice contributions, the

323   extracted β was used to determine the Debye temperature, Θ_D, yielding 278 K. This is in reasonable

324   agreement with the value of *Kobayashi et al.* (1999) (Θ_D = 313 K), who, we note, did not include

325   the higher order αT^5 term used here. We add that in our case the αT^5 term is indeed almost an order

326   of magnitude smaller than the βT^3 term, even at the highest T, as would be expected. Finally, with

327   respect to the excess specific heat at $T^2 < 30$ K^2 (i.e., below 5.5 K, as also seen in *Kobayashi et al.*

328   (1999)) we note only that upturns on $C_P(T)$ vs. T^2 plots at the lowest T are not at all uncommon in

329   solid-state systems, and can derive from Schottky anomalies, for example (*Rosenberg*, (1963);

330   *Gopal*, (1966)). The latter occur due to any mechanism that produces a manifold of low-lying

331   states, and can result from all manner of origins; further study at temperatures well below 1 K

332   could clarify this.

333   **2.4   MAGNETIC PROPERTIES**

334   **2.4.1   REMANENT AND INDUCED MAGNETIZATION**

335   In paleomagnetism, the Besnus transition is associated with a loss in remanent magnetization

336   on cooling. We measured the temperature dependence of a room temperature saturation isothermal

337   magnetization (RTSIRM) with a Quantum Design MPMS-XL (Magnetic Property Measurement

338   System) on cooling and warming. The specimen acquired a RTSIRM in a 2.5 T magnetic field at

339   300 K applied along two arbitrarily chosen directions in the basal plane of the crystal (Φ_1, Φ_2),

340   both roughly perpendicular to the [001] *c*-axis. The temperature dependence of the RTSIRM was

341   measured twice, firstly spanning the full temperature range from 300-10 K (5K/min) and secondly

342   in high resolution (0.5 K/min) spanning the transition (20-50 K).

343   The cooling path (Fig. 4 insets) of the RTSIRM (Φ_1 = 1.5, Φ_2 = 1.9 Am^2/kg) shows a gradual

344   decrease in magnetization to ≈ 45 % at 110-150 K, where it plateaus. Characteristic of the Besnus

15

Preprint submitted to American Mineralogist February 15, 2018

345   transition (*Dekkers et al.,* 1989), the remanence drops sharply in the narrow temperature range of

346   35-25 K (fig. 4). Estimates of the transition from the maximum dM/dT, yield a slightly higher

347   temperature (34 K) than the peak in specific heat (31.7 K). While the shapes of the cooling paths

348   in Φ_1 and Φ_2 are comparable, the warming paths (path 4 in Fig. 4a,b)) are quite different in the

349   vicinity of T_{Bes}, when measured in high-resolution (0.5 K steps). The recovery of magnetization

350   by warming back through the Besnus transition is strongly dependent on the grain-size of the

351   sample and should be low for large grains (Dekkers et al., 1989). Along Φ_1 (Fig. 4a) a small portion

352   ($\approx$ 5%) of the RTSIRM is recovered on warming from 10 K back to 40 K. In contrast, the

353   measurement along direction Φ_2 (Fig. 4b) shows a zig-zag behavior at T_{Bes}, with a local minimum

354   centered exactly at the specific heat peak. Furthermore, Φ_2 shows little remanence recovery.

355   Finally, the remaining remanence decays further with warming and only 20 ± 4 % of the initial

356   RTSIRM remains at room temperature.

357   *Dekkers et al. (1989)* showed that cycling to 4.2 K changes the median destructive field (MDF)

358   of the sample. Similarly, the second high resolution cooling/warming cycle (path 3,4) shows that

359   the newly acquired RTSIRM(50 K) is slightly larger than the first one. This indicates that the

360   changes occurring across the Besnus transition may not be entirely reversible. Furthermore, the

361   changes in MDF are grain-size-dependent *(Dekkers et al.,1989)*, with the biggest increases

362   occurring in larger particles. Thus, the configuration of domain walls in large, multi-domain grains

363   may be altered after cycling though the Besnus transition. A possible rearrangement of vacancies

364   at the transition could change the defect structure of the crystal and lead to different pinning of

365   domain walls and consequently a hardening of MDF and increased remanence ratio (Table 1).

366   The application of DC magnetic fields can modify the precise temperature of some magnetic

367   transitions, or even influence crystallographic changes during transitions in magnetic materials.

16

368   For example, in magnetite the orientation of the monoclinic *c*-axis below the Verwey transition

369   can be strongly controlled by the application of a DC magnetic field during cooling, where the

370   monoclinic *c*-axis is selected from the cubic *a*-axis that is closest to the orientation of the applied

371   field (*Li, 1932, Kasama et al., 2010*). To look for field-dependent effects at the Besnus transition,

372   we performed in-field cooling (FC) (5 K/min) in 0.5, 1, 1.5, 2 and 3 T (B⊥[001]) followed by zero-

373   field warming (5 K/min) of the low temperature remanence (LTSIRM) that was acquired in the

374   respective field at 10 K (Fig. 5). The saturation magnetization determined from field cooling

375   (M(300K, 3T) = 20.2 Am^2/kg, see table 1) is well within the range of reported values (18.3-21.2

376   Am^2/kg) (O'Reilly *et al.*, 2000; Kind *et al.*, 2013). As the sample cools in a field (Fig. 5a), the

377   magnetization increases to a local maximum at $T \approx 180$ K (M(180 K, 3 T) = 21.7 Am^2/kg). The

378   maximum is located close to where the magnetic anisotropy constant K_4 is also at a maximum and

379   where K_3 changes sign from positive to negative (*Bin and Pauthenet*, 1963).

380   Cooling in fields lower than ≈ 1.5 T causes a sharp increase of magnetization at the Besnus

381   transition. By comparison, in strong fields ($B > 1.5$ T), the Besnus transition is only visible as a

382   slight bump in the magnetization, which has been reported in several studies (*Besnus and Meyer*,

383   1964; *Dekkers et al.*, 1989; *Kind et al.*, 2013; *Charilaou et al.*, 2015; *Koulialias et al.*, 2016). The

384   changing crystalline anisotropy causes the spins, which are lying in the basal plane at room

385   temperature, to rotate out of the plane with decreasing temperature (*Bin and Pauthenet*, 1963;

386   Powell *et al.* 2004). Thus, the increase in magnetization could be related to a change in spin

387   configuration at the transition.

388   We can compare the directional dependence of the magnetization with data from magnetic

389   hysteresis loops (*Volk et al.*, 2016), which were measured as a function of orientation (Φ) and

390   temperature on a single crystal sister specimen from the same sample studied here. Consequently,

17

391   each magnetization value can be expressed as a function of field, orientation and temperature M

392   (B, T, Φ) and used to determine quasi "FC". Figure 5b shows the magnetization in a 500 mT field

393   in different crystallographic orientations as a function of temperature. Similar to the MPMS

394   measurements along Φ_1 and Φ_2 (Fig. 5a), the quasi FC data shows orientation-dependent

395   magnetization. However, these measurements show a clear directional dependence of the shape

396   and magnitude of the Besnus transition. Moreover, the standard deviation of the induced moment

397   is about 2.6 times greater for $T = 50$ K than for $T = 20$ K. The decrease in variability at lower

398   temperature suggests changes in magneto-crystalline anisotropy as the crystal is cooled through

399   the transition.

400   To check for possible thermal hysteresis, we repeated the FC experiment (500 mT, Φ_2) at a

401   higher resolution (0.5 K). While hysteretic behavior is typical for first-order transitions, no such

402   behavior is expected for second-order ones, as noted above. The fact that both cooling and

403   warming curves are perfectly aligned, completely reversible, and show no hysteresis (inset in Fig.

404   5b), further underlines the second-order character of the Besnus transition, consistent with our

405   specific heat data.

406   The remanence acquired in the field-cooling experiments at 10 K (LTSIRM, Fig. 5c) was

407   measured on warming back to room temperature in zero field. The absolute magnetization is the

408   same for all fields used, which drops by 90 % at T_{Bes} and further decays to only $\approx$ 2% at room

409   temperature. While the LTSIRM is about 7 times stronger than the RTSIRM (tab. 1) at low

410   temperature, the two are comparable after a full cooling-warming circle. There was no field

411   dependence observed in the warming of LTSIRM for pure 4C pyrrhotite.

412

413   The $M(B,T,\Phi)$ data (Fig. 5b) from the hysteresis loops, as described earlier, allow for the

414   extraction of T_{Bes} as a function of Φ (in the basal plane) and applied field. We define $T_{\mathrm{Bes}}(B, \Phi)$ as

415   the maximum change in magnetization $(\max(dM/dT))$ on cooling. $T_{\mathrm{Bes}}(B, \Phi)$ is determined from

416   a cubic spline interpolation of the smoothed data. Figure 6a shows that the mean $T_{\mathrm{Bes}}(\Phi)$ is field

417   dependent, and increases from ~30 to ~34 K as applied field increases from 0 to 1 T. The most

418   prominent change is visible in the first 100 mT (see inset in Fig. 6a), where T_{Bes} changes by ≈ 2 K

419   from 30 K to 32 K. As the field is further increased, T_{Bes} rises linearly until it saturates at 750 mT

420   and 34 K. In our previous study (*Volk et al.,* 2016), we were not able to explain how the coercivity

421   of remanence (B_{cr}) of the single crystal could be lower than its coercivity (B_{c}) for temperatures

422   < 30 K. However, the field dependence of the transition can explain this phenomenon. When B_{cr}

423   is measured in zero field, the crystal is above T_{Bes} and consequently the coercivity of remanence

424   is low. B_{c}, on the other hand, is measured *in* a magnetic field, which raises T_{Bes}. The measurement

425   is therefore done below the transition temperature. B_{c} is greatly enhanced for T $< T_{\mathrm{Bes}}$ which leads

426   to the unusual $B_{\mathrm{cr}} < B_{\mathrm{c}}$. Furthermore, the mean $T_{\mathrm{Bes}}(B)$ shows a directional dependence (Fig. 6b).

427   Parallel to the crystallographic *a*-axes (determined using EBSD (see *Volk et al.*, 2016)), we find

428   the maximum T_{Bes}, while minima lie between axes, coinciding with orientations whose hysteresis

429   loops most strongly show a second inflection. Finally, combining the field and directional

430   dependence (Fig. 6c) shows the minimum (dark color) of T_{Bes} (30.1 K) located close to the

431   projection of the *c*-axis onto the basal plane with a transition temperature close to the peak in heat

432   capacity. Thus, the highest Besnus transition temperatures occur when a field is applied parallel to

433   one of the *a*-axis directions, while the lowest T_{Bes} occurs in between these directions and closest

434   to the projection of the *c*-axis. It appears as though the application of DC magnetic fields in

19

435   between the *a*-axes, or even potentially along the c-axis, stabilizes the $T > T_{Bes}$ phase, requiring

436   lower temperatures to ultimately bring about the Besnus transition.

2.4.2   ALTERNATING CURRENT SUSCEPTIBILITY

438   Measurements of low-field AC susceptibility as a function of temperature can provide

439   important information about the mobility of domain walls as a mineral's intrinsic magnetic

440   anisotropy changes, as the pinning energies of vacancies change, or as a mineral undergoes a

441   crystallographic transition. Low field in-phase (χ') and out of phase (χ'') AC susceptibility

442   between 10 K and 300 K (see table 2) was collected at 5 field amplitudes (0.02 - 0.3 mT, 5K/min)

443   on cooling and subsequent warming along the sample's [001] axis ($\chi_\parallel$) as well as perpendicular to

444   it ($\chi_\perp$, Φ_2). The AC susceptibility (Fig. 7) in the basal plane ($\chi_\perp$) shows a gradual decline during

445   cooling until it drops sharply at $\approx$ 34 K. There is a strong amplitude dependence in both the in-

446   phase (Fig. 7a) and the out-of-phase components (Fig. 7b) of $\chi_\perp$. While the amplitude dependence

447   of $\chi_\perp$ is approximately constant down to 35 K, it increases dramatically at T_{Bes} and then drops to

448   close to zero below the transition. The measurement of $\chi_\parallel$, on the other hand, shows a vastly

449   different behavior. Here, both $\chi_\parallel$ and its amplitude dependence decrease with increasing

450   temperature. The maximum of $\chi_\parallel$ (17-24 $\times$ $\chi_\parallel(T_R)$) is reached close to the Besnus transition. Similar

451   to $\chi_\perp$, $\chi_\parallel$ evidences a sharp change at T_{Bes}. While the measurements in this study come from a

452   multidomain single crystal, *Kind et al.* (2013) measured similar changes in susceptibility for a

453   natural Fe_7S_8 powder. They interpret the decrease in susceptibility during cooling across the

454   Besnus transition as a reduction in domain wall mobility at lower temperatures, an explanation

455   which would only apply to predominantly MD samples. *Bezaeva et al.,* (2016) also reported a drop

456   in susceptibility across the Besnus transition for predominantly single-domain 4C pyrrhotite,

20

457   which suggests instead that something about the intrinsic magnetic anisotropy energy of the

458   material has changed below T_{Bes}.

459   To gain a better understanding of how susceptibility changes at the transition, we also

460   measured the frequency dependence of AC susceptibility ($\chi_\perp$ and $\chi_\parallel$) at high resolution (0.5 K

461   steps) for 7 frequencies (1 - 1000 Hz) spanning T_{Bes} (from 20-40 K). There is no frequency

462   dependence in the in-phase data (Fig. 6a) for either $\chi_\perp$ or $\chi_\parallel$. There is a slight frequency dependence

463   in the out-of-phase data (Fig. 6b), however, the main drop of $\chi_\parallel$ occurring at temperatures ≈1 K

464   warmer than $\chi_\perp$ in both in-phase and out-of-phase measurements. This shift is reproducible and is

465   likely not an instrumental artifact. Furthermore, close inspection of the data of *Koulialias et al.*

466   (2016) reveals a similar shift, which seems to decrease with increasing frequency.

467   A prominent secondary peak is visible at ≈ 32 K (see inset in Fig. 7a) in $\chi_\perp$' and less expressed

468   in $\chi_\perp$", while $\chi_\parallel$ does not show it at all. Similar features were reported by *Koulialias et al.* (2016)

469   in their natural single crystal and *Kind et al.* (2013) in Fe_7S_8 powder. To resolve this feature, data

470   must be collected at sufficiently high resolution (here, 0.5 K steps). Thus, the feature is not visible

471   in the lower resolution amplitude dependence measurements (2.5 K steps). It is noteworthy that

472   this secondary peak is located directly at the temperature of the specific heat peak discussed above.

473   This indicates that the peak is directly related to the transition. Consequently, a Besnus transition

474   temperature, determined from the decay of susceptibility may be overestimating T_{Bes}.

475   The strong anisotropy of susceptibility in 4C pyrrhotite is reflected in the vastly different

476   susceptibilities that are measured parallel and perpendicular to [001]. At room temperature, $\chi_\perp$ is

477   ~170 times larger than $\chi_\parallel$. As temperatures approach T_{Bes}, however, $\chi_\parallel$ increases while $\chi_\perp$ decreases,

478   which results in a linear decrease of their ratio ($\chi_\perp / \chi_\parallel$) when plotted logarithmically (Fig. 8). This

21

479 linearity is broken at T_{Bes}, where the ratio shows a discontinuity, again well-aligned with the

480 specific heat peak (see inset Fig. 7). We interpret this change a consequence of the rotation of the

481 easy axis of the crystal during cooling. *Powell et al.* (2004) showed that as Fe_7S_8 is cooled, the

482 easy axis rotates out of the (001) plane, consistent with increasing susceptibility in [001]. Similarly,

483 the sudden increase in $\chi_{\perp/}\chi_{\parallel}$ could be caused by an abrupt rotation of the easy axis towards the

484 basal plane and back out, towards [001].

485 Finally, below T_{Bes}, $\chi_\perp$ decreases to <1% of its room temperature value (Table 2); $\chi_\parallel$ on the

486 other hand is only reduced to about 50%. Consequently, below the transition both susceptibilities

487 are comparable ($\chi_\perp \approx 2 \times \chi_\parallel$). Thus, the anisotropy of the crystal is greatly reduced below T_{Bes}. The

488 sample in study has a platelet shape, and therefore shape anisotropy may play a role. If one were

489 to correct for the shape of our sample, the sense of the correction would lower the susceptibility

490 within the basal plane, and therefore it is possible that susceptibility parallel to [001] could be even

491 closer to, if not larger than, $\chi_\perp$.

492 **2.5 ELECTRICAL RESISTIVITY**

493 To gain an understanding of the electronic property changes that take place across the Besnus

494 transition, we performed temperature- and magnetic-field-dependent measurements of resistivity

495 (ρ) from 4 to 300 K, using a home-built Janis cryostat with a 9 T superconducting magnet. Silver

496 paste contacts were employed in a 4-wire van der Pauw configuration (*van der Pauw*, 1958), using

497 a Lakeshore 370 13.7 Hz AC bridge to measure 4-terminal resistances. Checks for Ohmicity,

498 contact resistance, and self-heating were made at 4 and 300 K.

499 As shown in Fig. 9a, the ρ in the basal plane of our 4C pyrrhotite single crystal exhibits clearly

500 metallic behavior ($d\rho/dT$ is metallic-like (i.e., positive) over almost the entire temperature range,

501 with finite apparent conductivity as $T \rightarrow 0$), with a large anomaly visible at 32 K, where the

22

Preprint submitted to American Mineralogist February 15, 2018

502   resistivity drops significantly. We note that the peak in the ratio of $\chi_{\parallel} / \chi_{\perp}$, this resistivity anomaly,

503   and the peak in specific heat are all located at the same temperature. This highlights the

504   reproducibility and precision of T_{Bes} in our measurements, in addition to its clear, recognizable

505   effect on diverse properties (magnetic, electronic, and thermodynamic). In contrast to the Verwey

506   transition in magnetite, which displays a sharp drop in resistivity on warming (e.g., *Kuipers and*

507   *Brabers, 1979*), the resistivity change here is continuous, again consistent with second-order

508   character of the Besnus transition (there is also no thermal hysteresis in $\rho(T)$ on heating/cooling).

509   The room temperature resistivity ($\rho_{300\ K}$) of the crystal measured here is 0.32 mΩ cm, which

510   compares well with the $\rho_{300\ K}$ of 0.41 mΩ cm originally obtained by *Besnus and Meyer* (1964),

511   being considerably lower than the 2.1 mΩ cm obtained by *Charilaou et al.* (2015). This

512   consistency with the original work, and the lower values than those obtained by *Charilaou et al.*

513   (2015), again highlight the quality of this phase-pure natural single crystal, and reinforce the clear

514   expression of the Besnus transition in this phase-pure sample. Consistent with this, the temperature

515   dependence of ρ is also stronger in this crystal. For example, the residual resistivity ratio (RRR),

516   defined as RRR = $\rho_{300\ K}/\rho_{5\ K}$, is 4.04 in this work, compared to ~2.9 in *Besnus and Meyer* (1964),

517   and 1.34 in *Charilaou et al.* (2015). This indicates not only lower defect densities in our phase-

518   pure crystal, but also a stronger decrease in $\rho(T)$ below T_{Bes}. With a RRR of above 4, and also

519   given the absolute magnitudes of the resistivities, this pyrrhotite crystal can be considered a "bad"

520   or "dirty" metal or semimetal. In terms of constraining the *origin* of the Besnus transition, we note

521   that any explanation for it must be able to explain a substantial *decrease* in resistivity on cooling.

522   Fig. 9b shows the magnetic field dependence of ρ vs. T around the Besnus transition, with the

523   field applied along a random direction in the basal plane. As the field increases from 0 T to 0.5 T,

524   progressive smearing of the sharp anomaly in ρ vs. T and a weak negative magnetoresistance (MR)

23

525   is seen, meaning that the apparent T_{Bes} increases monotonically with field, consistent with

526   magnetization data shown in Fig. 6a. In this field orientation, there is no significant additional field

527   dependence above 0.5 T. This can be seen in the inset to Fig. 9c, where the magnetoresistance (MR

528   = ($\rho(H)$ - $\rho(0)$) / $\rho(0)$) as a function of magnetic field at 32 K only shows negative MR out to ~1

529   T. Application of larger fields then causes an inversion in the slope of the MR and a slight increase

530   in magnitude, saturating at high fields. The main panel of Fig 9c shows MR(9 T) as a function of

531   temperature. Upon warming, positive MR at low T gives way to a slight negative MR around T_{Bes},

532   with the peak negative MR being ~ -2% at T_{Bes}. Above the transition, the MR goes positive again,

533   and remains relatively constant past 60 K at about ~0.5%. In this field orientation, MR effects are

534   thus small, the typical growth of positive MR on cooling, as expected in a metal, being interrupted

535   at T_{Bes} with only a small negative MR effect. This small negative MR saturates quickly with

536   increasing field.

537   Fig. 9d displays the magnetic field dependence of ρ vs. T around the Besnus transition, this

538   time with the field applied *out* of the basal plane, i.e., parallel to the *c*-axis. In this case, a clear

539   decrease in the apparent transition temperature is observed as the out-of-plane magnetic field is

540   increased from 0 to 9 T. The apparent transition temperature shift is monotonic, with an overall

541   shift of ~2 K with 9 T of applied field, which is relatively small. The presence of an out-of-plane

542   field thus apparently favors the $T > T_{Bes}$ phase. Importantly, this is consistent with the remanence

543   and hysteresis data (§2.4.1) (Fig. 6c) in that when the applied field is along, or parallel to, the c-

544   axis, the lowest T_{Bes} values are observed. Specifically, it appears that fields applied parallel to the

545   *c*-axis pull the spins out-of-plane near the transition, which allows the phase above the transition

546   to persist to lower T. One way to rationalize this is in terms of Zeeman energy stabilization. The T

547    $> T_{Bes}$ phase has a larger component of magnetization along the c-axis than the $T < T_{Bes}$ phase (see

24

548 *Charilaou et al.* (2015)), allowing the $T > T_{Bes}$ phase to be stabilized when a field is applied along

549 the c-axis, lowering T_{Bes} as larger fields are applied. Naturally, and as shown in the expanded view

550 in Fig. 9d, the lowering of the apparent transition temperature with out-of-plane field combines

551 with the positive $d\rho/dT$ to generate positive MR. This is shown as a function of magnetic field at

552 30 K in the inset to Fig. 9e, where positive MR up to 7.5 % is seen, not saturating even at 9 T. Fig.

553 9e shows that this positive MR is found at all temperatures between $5 - 60$ K when the field is

554 applied parallel to the *c*-axis. The positive MR effect associated with the Besnus transition turns

555 on near T_{Bes}, reaches a sharp peak, and then gradually decreases towards 5 K.

556 **3   DISCUSSION**

557 This study represents one of the most exhaustive studies of the Besnus transition to date,

558 performed on a high purity, phase-pure, 4C pyrrhotite single crystal specimen. While the precise

559 mechanism(s) driving the transition still remain elusive, it is possible to now better constrain

560 potential explanations by considering all of the phenomena that have been observed to accompany

561 the transition. Ultimately, a comprehensive theory for the Besnus transition must explain:

562 1.   An entropy change at T_{Bes} resulting from an apparently second-order phase transition in

563   specific heat (this study, *Grønvold et al., 1959*)

564 2.   Loss of remanent magnetization upon cooling (RTSIRM) and warming (LTSIRM) through

565   the transition.

566 3.   Changing rock magnetic properties (B_c, B_{cr}, M_{rs}), while M_s remains constant

567 4.   Irreversible changes after cycling through T_{Bes}, represented as increases in remanence and

568   MDF (this study, *Dekkers et al., 1989*)

569 5.   The disappearance of the second inflection phenomenon in hysteresis loops at T_{Bes} (appears

570   at $\approx 200K$, aligned with crystal structure) (*Volk et al., 2016, Koulialias at al., 2016*)

571   6. Symmetry changes of rock magnetic properties from 6-fold above the transition to 4-fold

572   below the transition (*Wolfers et al., 2011, Volk et al., 2016, Koulialias et al., 2018*)

573   7. Field dependence of $T_{Bes} \perp [001]$, as determined from magnetic data and resistivity

574   8. Field dependence of T_{Bes} in resistivity $\| [001]$

575   9. Different magnetoresistive behavior when applied fields are within the basal plane or

576   parallel to the *c*-axis

577   10. A distinct decrease in resistivity on cooling through T_{Bes}

578   11. Splitting of Fe sites (4 unique $\rightarrow$ 5 unique) below T_{Bes}, as determined by Mössbauer

579   spectroscopy (*Jeandey et al., 1991, Oddou et al., 1992*)

580   12. The anomaly seen in short-range magnetic scattering seen in SANS data.

581   Unfortunately, no single mechanism appears capable of simply explaining all of the observed

582 behaviors across the transition, although existing observations do allow us to rule out some

583 proposed mechanisms, which ultimately helps constrain the nature of the transition. All of the

584 mechanisms proposed thus far are discussed in turn below in addition to several new ones.

585   *3.1 The role of interacting superstructures.* The specimen studied here is purely 4C pyrrhotite

586 and contains *no additional superstructures*, as supported by powder X-ray diffraction, microprobe

587 analysis, heat capacity measurements, a single magnetic ordering temperature, the absence of a

588 magnetic λ-transition, the M_s value, and the RRR value. Nevertheless, we clearly observe the

589 Besnus transition in all physical properties studied. The specific heat shows a clear peak at ≈ 31.7

590 K, in agreement with the transition temperature determined from resistivity measurements to

591 within one kelvin at zero field. This agrees well with that of the synthetic specimen studied by

592 *Grønvold et al.* (1959). The transition temperatures in the magnetic susceptibility, RTSIRM,

593 LTSIRM, and FC curves (≈ 32 - 34 K) are slightly higher than the C_p peak, but agree well with

26

594   most published data (*Dekkers et al.*, 1989; *Rochette et al.*, 1990; *Fillion and Rochette*, 1988; *Kind*

595   *et al.*, 2013). On the other hand, the 26 K transitions described by *Charilaou et al.* (2015) and

596   *Koulialias et al.* (2016) deviate markedly. *Baranov et al.* (2014) showed that Ti substitution can

597   induce changes in vacancy ordering, which results in a change from 4C to 3C in Fe_7S_8.

598   Consequently, it seems possible that the 0.5 % Ni substitution in their sample may be responsible

599   for the additional 5C* structure, and may explain the shifted transition temperature and the

600   suppressed specific heat peak. More substantial Ni substitution results in an entirely new iron

601   sulfide mineral Smythite $(Fe,Ni)_9S_{11}$ with a trigonal structure, that is often found associated with

602   pyrrhotite. We conclude that the Besnus transition is intrinsic to the 4C phase, and is not caused

603   by interactions of different superstructures as proposed by *Koulialias et al.* (2016, 2018).

604   ***3.2 The role of twinning.*** Pyrrhotite is prone to the formation of stacking faults and twins when

605   there are local perturbations in the superstructure (*Bin and Pauthenet, 1963*). Thus, one could

606   imagine that even subtle changes to the unit cell across the Besnus transition may induce twinning

607   at the nanometer scale (*Wolfers et al., 2011*). The formation of such features could also reconfigure

608   the distribution of dislocations, vacancies, and pinning sites for domain walls within the material.

609   Consequently, the magnetic interactions between these twins would change, as well as the mobility

610   of domain walls, and thus, the bulk magnetic properties would also change. Nanometer-scale

611   twinning may explain the irreversible changes (e.g., enhanced remanence and coercivity) seen after

612   low temperature cycling. Twinning is also consistent with the length scale of the

613   structural/magnetic changes observed in our high Q SANS data (Figure 2(c,d)), but is somewhat

614   inconsistent with the significant decrease in resistance observed below the transition. The

615   decreasing resistivity can perhaps only be explained by a reduction in the number of twins.

616   Furthermore, twinning is not able to explain the splitting of the occupancy of Fe sites observed in

27

617   the Mössbauer data. The orientation of twinning in other magnetic minerals, such as magnetite,

618   can be influenced by applied fields, and if this were the case for pyrrhotite, it could explain the

619   field dependence of the transition. Depending on the orientation of the twin boundaries, it is

620   possible that the symmetry of the magnetic properties may change from 6-fold to 4-fold below the

621   transition. As a mechanism, twinning could thus potentially explain many of the phenomena

622   observed below the Besnus transition.

623   ***3.3 The role of crystallographic transitions.*** Wolfers *et al*. (2011) not only proposed a change

624   in twinning schemes, but a true crystallographic transition, with a lowering of the symmetry from

625   monoclinic to triclinic. This is consistent with the changes in the symmetry of rock magnetic

626   properties from 6-fold symmetry above T_{Bes} to 4-fold symmetry below T_{Bes} (*Volk et al.,* 2016).

627   Confusingly, however, our SANS data show a clear six-fold symmetry, even at 5 K. While this is

628   not conclusive evidence against a crystallographic transition, it indicates that any crystallographic

629   changes, if they occur, could be weak. It is worth reiterating in this regard that the 4C monoclinic

630   superstructure at room temperature is only 0.26° different from a perfect hexagonal unit cell

631   (*Wolfers et al.,* 2011). Hence, any additional subtle distortions may not be easily detectable, and

632   will require further high-resolution crystallographic study.

633   A crystallographic change, where the monoclinic unit cell is subtly distorted to form a

634   different, also monoclinic unit cell is another possible mechanism. Such an *isostructural* or

635   *isomorphic* transformation would be difficult to detect with SANS. However, such a transition

636   could explain many of the phenomena described above. The changing crystal structure could

637   explain the second-order transition indicated by specific heat, but only if the phase transition is

638   truly second-order, or only very weakly first-order. A change in crystal structure would result in

639   changes in the band structure of the material, which would affect electronic transport, *i.e.*, the

28

640   resistivity and MR. Therefore, the differences in electronic transport (specifically $d\rho/dT$) above

641   and below T_{Bes} could potentially be explained. Furthermore, the newly created twins could change

642   the domain structure and pin magnetic domain walls at twin boundaries. Consequently, the

643   changing unit cell and rearrangement of domains would lead to a loss of the remanent

644   magnetization. Pinning of domain walls, on the other hand, would increase the coercivity of the

645   crystal. If the changes are small enough, the saturation magnetization should not be affected.

646   Finally, the generation of twins that accompanies an isostructural transformation could explain

647   irreversible changes on cycling through the transition.

648   ***3.4 The role of changing crystalline anisotropy.*** Several studies have investigated the

649   crystalline anisotropy of pyrrhotite (*Mikami et al. 1959;* Bin and Pauthenet, *1963; Sato et al.,*

650   *1964*). Bin and Pauthenet (*1963*) showed that the crystalline anisotropy of pyrrhotite changes upon

651   cooling. The K_4 anisotropy constant, which dominates, shows a maximum, while the K_3 constant

652   changes sign and becomes negative at ≈ 200 K. The changing anisotropy causes the spins to rotate

653   out of the basal plane, which was confirmed by neutron diffraction data by Powell *et al.* (*2004*).

654   These changes in magnetic anisotropy may be able to explain the Besnus transition. In this

655   scenario, the magnetic easy axis switches to a different crystallographic direction. Consequently,

656   the remanent magnetization would be lost and domain wall orientation as well as the fundamental

657   magnetic properties would change. However, the measurements of Bin and Pauthenet (*1963*) were

658   done on an obviously twinned crystal. Furthermore, the authors were not able to determine the

659   anisotropy from measurements in the basal plane at temperatures < 60 K, as the magnetic easy axis

660   seemed to switch when a magnetic field is applied. As the second inflection in magnetic hysteresis

661   loops appears at ≈ 180 K, it is likely related to this presumed easy axis switching.

662   On balance, it seems unlikely that the Besnus transition is solely caused by a changing

663   anisotropy. Given that the low temperature behavior of the crystalline anisotropy is not well

664   known, the main changes seem appear at 200 K. However, the remanence is unaffected, as are the

665   magnetic properties. Furthermore, the model fails to explain the changes seen in resistivity,

666   Mössbauer, and high Q (Lorentzian) SANS. On the other hand, it seems likely that the anisotropy

667   would change as a byproduct of even a subtle crystallographic transition.

668   **3.5 The role of exchange inversion within NiAs structures.** Kittel (*1960*) predicted a

669   phenomenon called exchange inversion in materials with a NiAs crystal structure. Since then it

670   has been found in Mn_2Sb and other Mn-Sb compounds with substitutions (e.g. *Bither et al., 1962*).

671   At the phase transition, the formerly ferromagnetic coupling between spins switches, and becomes

672   antiferromagnetic. The spins within each Fe plane in pyrrhotite couple ferromagnetically, while

673   the spins between layers couple antiferromagnetically. It seems possible for exchange inversion to

674   take place at T_{Bes}. This would change the coupling within a plane to become antiferromagnetic,

675   becoming ferromagnetic to the adjacent plane. The changing spin orientation would remove most

676   of the remanent magnetization, without affecting the bulk saturation magnetization. The field

677   dependence of the transition could also be explained, as strong magnetic fields could exert force

678   on the spins and hinder their reorganization. Furthermore, a reorientation of spins was found to

679   change electronic properties in a pyrrhotite analogue Fe_7Se_8 with a 4C NiAs structure (*Li et al.,*

680   *2016*). While being able to explain several phenomena, this scenario fails to explain the splitting

681   of the iron sites in Mössbauer spectroscopy. Furthermore, a spin reorganization should be visible

682   in neutron diffraction data. Powell *et al.* (2004) did not observe such a transition in their neutron

683   study. However, in their work only one scan was taken below T_{Bes}.

30

684   ***3.6 Future research.*** In light of the above, this study clearly emphasizes the need for further

685   research along at least three lines: High-resolution structural characterization, laboratory synthesis

686   of single phase pyrrhotite, and linking single crystal observations to bulk sample behavior. The

687   observations in this study and previous work suggest that nanometer-scale twinning within

688   pyrrhotite across the Besnus transition may explain many of the magnetic and physical properties

689   observations. However, it is not clear which mechanism(s) may be driving the twinning. To

690   distinguish between subtle crystallographic transitions or fundamental changes in the exchange

691   coupling, further research is required. Wolfers *et al.* (2011) proposed that fine low temperature X-

692   ray diffraction experiments could be used to obtain a detailed description of any crystallographic

693   change near the 32 K transition. If such an approach is meant to differentiate between monoclinic-

694   triclinic and isostructural transitions, then these diffraction experiments may only be possible using

695   synchrotron facilities. Similarly, synchrotron-based X-ray absorption near-edge structure

696   (XANES) analyses may shed light on the changes in Fe site occupancy across the transition

697   originally observed with Mössbauer spectroscopy. Finally, powder neutron diffraction, similar to

698   Powell et al. (2004) at temperatures spanning the transition would further show changes in spin

699   structure as well as possible structural changes.

700   Magnetic methods may also help constrain the importance of twinning in mixed phase

701   (hexagonal and monoclinic) crystals. If nanometer-scale twinning does occur across the Besnus

702   transition, then vacancies may reorder on warming, and the distribution of pyrrhotite

703   superstructures at room temperature may change after cycling through the Besnus transition. If so,

704   then there should be observable changes in the nature of the lambda transition near 220°C in

705   susceptibility measurements. Given the field dependence of the Besnus transition observed here,

706   it is possible that fields applied along different crystallographic directions may lead to different

Preprint submitted to American Mineralogist February 15, 2018

707 ratios of superstructures at room temperature. However, if no lambda transition is observed near

708 220°C after cycling through the Besnus transition, then perhaps the role of twinning may need to

709 be re-evaluated.

710 **4   IMPLICATIONS**

711 Many open questions also remain regarding the influence of the Besnus transition on the full-

712 vector remanence held by pyrrhotite in natural samples. While the magnitude of magnetization

713 decreases after cycling through the Besnus transition, the direction of a laboratory-induced

714 isothermal remanent magnetization in a single crystal of pyrrhotite is stable (Feinberg *et al.*, 2015).

715 This observation may have important implications for paleomagnetic studies of terrestrial and

716 meteoritic samples containing pyrrhotite. Similar to the ways in which low-temperature treatments

717 that cycle through the Verwey transition in magnetite are used to reduce the remanence held by

718 large multidomain grains and give a more unfettered view of the remanence held by well-behaved,

719 single-domain-like grains, cycling through the Besnus transition may be useful isolating high

720 coercivity remanence in pyrrhotite. Single-domain-like grains also express a Besnus transition, but

721 no observations exist regarding the directional stability of their magnetization across the transition.

722 The high purity of the 4C single crystal sample in this study is particularly unusual but was

723 essential for demonstrating the intrinsic nature of the Besnus transition and its directional

724 dependence. However, this sample is limited in mass, and, given the numerous ongoing questions

725 about pyrrhotite, there is a clear need to develop dependable synthesis methods (metastability is

726 often a problem) for pyrrhotite that control the resulting superstructures. Many existing synthesis

727 methods are time consuming, require repeated annealing steps (which only partially control the

728 ratio of resulting superstructures), and are limited to only producing fine grained samples. Methods

32

729 capable of producing large single crystals of well-characterized pyrrhotite would be especially

730 beneficial to future research.

731   In addition, due to our improved ability to detect pyrrhotite in natural samples, it is becoming

732 increasingly important to identify how this mineral influences or records numerous geophysical,

733 environmental, and planetary science processes. Similarly, the mineral and its superstructures are

734 important to the materials science community. A deeper understanding of the nature of the Besnus

735 transition will only improve our interpretations regarding pyrrhotite, and we hope this study makes

736 a convincing case for the need for further research that combines high-resolution structural

737 characterization with carefully controlled rock magnetic experiments on natural and synthetic bulk

738 samples.

750

Preprint submitted to American Mineralogist February 15, 2018

751   **6   REFERENCES**

752   Arnold, R.G. (1967) Range in composition and structure of 82 natural terrestrial pyrrhotites.

753   The Canadian Mineralogist, 9, 31–50.

754   Aubourg, C., and Pozzi, J.-P. (2010) Toward a new <250°C pyrrhotite–magnetite

755   geothermometer for claystones. Earth and Planetary Science Letters, 294, 47–57.

756   Baranov, N.V., Ibrahim, P.N.G., Selezneva, N.V., Kazantsev, V.A., Volegov, A.S., and

757   Shishkin, D.A. (2014) Crystal structure, phase transitions and magnetic properties of pyrrhotite-

758   type compounds Fe7−xTixS8. Physica B: Condensed Matter, 449, 229–235.

759   Bertaut, E.F. (1953) Contribution à l'étude des structures lacunaires: la pyrrhotine. Acta

760   Crystallographica, 6, 557–561.

761   Besnus, M.J., and Meyer, A.J. (1964) Nouvelles données expérimentales sur le magnétisme de

762   la pyrrhotine naturelle. Proc. Int. Conf. Mag., 20, 507–511.

763   Bezaeva, N.S., Chareev, D.A., Rochette, P., Kars, M., Gattacceca, J., Feinberg, J.M., Sadykov,

764   R.A., Kuzina, D.M., and Axenov, S.N. (2016) Magnetic characterization of non-ideal single-

765   domain monoclinic pyrrhotite and its demagnetization under hydrostatic pressure up to 2 GPa with

766   implications for impact demagnetization. Physics of the Earth and Planetary Interiors, 257, 79–90.

767   Bin, M., and Pauthenet, R. (1963) Magnetic Anisotropy in Pyrrhotite. Journal of Applied

768   Physics, 34, 1161–1162.

769   Bither, T.A., Walter, P.H.L., Cloud, W.H., Swoboda, T.J., and Bierstedt, P.E. (1962) New

770   Modified Mn2Sb Compositions Showing Exchange Inversion. Journal of Applied Physics, 33,

771   1346–1347.

772   Cantu, J., Gonzalez, L.E., Goodship, J., Contreras, M., Joseph, M., Garza, C., Eubanks, T.M.,

773   and Parsons, J.G. (2016) Removal of arsenic from water using synthetic Fe_7S_8 nanoparticles.

774   Chemical Engineering Journal, 290, 428–437.

775   Charilaou, M., Kind, J., Koulialias, D., Weidler, P.G., Mensing, C., Loffler, J.F., and Gehring,

776   A.U. (2015) Magneto-electronic coupling in modulated defect-structures of natural $Fe_{1-x}S$.

777   Journal of Applied Physics, 118, 083903–6.

778   Dekkers, M.J. (1988) Magnetic properties of natural pyrrhotite Part I: Behaviour of initial

779   susceptibility and saturation-magnetization-related rock-magnetic parameters in a grain-size

780   dependent framework. Physics of the Earth and Planetary Interiors, 52, 376–393.

781   Dekkers, M.J., Mattéi, J.-L., Fillion, G., and Rochette, P. (1989) Grain-size dependence of the

782   magnetic behavior of pyrrhotite during its low-temperature transition at 34 K. Geophysical

783   Research Letters, 16, 855–858.

784   Dunlop, D.J. (2002) Theory and application of the Day plot (Mrs/Ms versus Hcr/Hc) 1.

785   Theoretical curves and tests using titanomagnetite data. Journal of Geophysical Research: Solid

786   Earth, 107, 2056.

787   Dunlop, D.J., and Özdemir, Ö. (1997) Rock Magnetism. Cambridge University Press,

788   Cambridge.

789   Erd, R.C., Evans, H.T., and Richter, D.H. (1957) Smythite, a New Iron Sulfide, and Associated

790   Pyrrhotite From Indiana. American Mineralogist, 42, 309–333.

791   Ericsson, T., Amcoff, Ö., and Nordblad, P. (1994) Vacancy ordering in Fe_7Se_8-Fe_7S_8 solid

792   solutions studied by Mössbauer, X-ray and magnetization techniques. Hyperfine Interactions, 90,

793   515–520.

35

794   Fegley, B., Jr., Lodders, K., Treiman, A.H., and Klingelhöfer, G. (1995) The Rate of Pyrite

795   Decomposition on the Surface of Venus. Icarus, 115, 159–180.

796   Feinberg, J.M., Solheid, P.A., Swanson-Hysell, N.L., Jackson, M.J., and Bowles, J.A. (2015)

797   Full vector low-temperature magnetic measurements of geologic materials. Geochemistry,

798   Geophysics, Geosystems, 16, 301–314.

799   Fillion, G., and Rochette, P. (1988) The Low Temperature Transition In Monoclinic Pyrrhotite.

800   Le Journal de Physique Colloques, 49, C8–907–C8–908.

801   Gilder, S.A., Egli, R., Hochleitner, R., Roud, S.C., Volk, M.W.R., Le Goff, M., and de Wit,

802   M. (2011) Anatomy of a pressure-induced, ferromagnetic-to-paramagnetic transition in pyrrhotite:

803   Implications for the formation pressure of diamonds. Journal of Geophysical Research: Solid

804   Earth, 116, B10101.

805   Gillard, T.M., Phelan, D., Leighton, C., and Bates, F.S. (2015) Determination of the Lamellae-

806   to-Disorder Heat of Transition in a Short Diblock Copolymer by Relaxation Calorimetry.

807   Macromolecules, 48, 4733–4741.

808   E. S. R. Gopal (1966) Specific Heats at Low Temperatures, Plenum Press, New York

809   Grønvold, F., Stølen, S., Labban, A.K., and Westrum, E.F. (1991) Thermodynamics of iron

810   sulfides I. Heat capacity and thermodynamic properties of Fe9S10 at temperatures from 5 K to 740

811   K. The Journal of Chemical Thermodynamics, 23, 261–272.

812   Grønvold, F., Westrum, E.F., and Chou, C. (1959) Heat Capacities and Thermodynamic

813   Properties of the Pyrrhotites FeS and Fe0.877S from 5 to 350°K. The Journal of Chemical Physics,

814   30, 528–531.

36

Preprint submitted to American Mineralogist February 15, 2018

815   Halgedahl, S.L., and Fuller, M.D. (1981) The dependence of magnetic domain structure upon

816   magnetization state in polycrystalline pyrrhotite. Physics of the Earth and Planetary Interiors, 26,

817   93–97.

818   Herndon, J.M., Rowe, M.W., Larson, E.E., and Watson, D.E. (1975) Origin of magnetite and

819   pyrrhotite in carbonaceous chondrites. Nature, 253, 516–518.

820   Jeandey, C., Oddou, J.L., Mattéi, J.-L., and Fillion, G. (1991) Mössbauer investigation of the

821   pyrrhotite at low temperature. Solid State Communications, 78, 195–198.

822   Kasama, T., Church, N.S., Feinberg, J.M., Dunin-Borkowski, R.E., and Harrison, R.J. (2010)

823   Direct observation of ferrimagnetic/ferroelastic domain interactions in magnetite below the

824   Verwey transition. Earth and Planetary Science Letters, 297, 10–17.

825   Kind, J., Garcia-Rubio, I., Charilaou, M., Nowaczyk, N.R., Loffler, J.F., and Gehring, A.U.

826   (2013) Domain-wall dynamics in 4C pyrrhotite at low temperature. Geophysical Journal

827   International, 195, 192–199.

828   Kittel, C. (1960) Model of Exchange-Inversion Magnetization. Physical Review, 120, 335–

829   342.

830   Kobayashi, H., Nozue, T., Matsumura, T., Suzuki, T., and Kamimura, T. (1999) The low-

831   temperature specific heat of FeS and M 0.875X (M = Fe, Co; X = S, Se) with a NiAs-like structure.

832   Journal of Physics: Condensed Matter, 11, 8673–8679.

833   Koulialias, D., Charilaou, M., Schäublin, R., Mensing, C., Weidler, P.G., Loffler, J.F., and

834   Gehring, A.U. (2018) Ordered defects in Fe 1− xS generate additional magnetic anisotropy

835   symmetries. Journal of Applied Physics, 123, 033902–11.

37

836   Koulialias, D., Kind, J., Charilaou, M., Weidler, P.G., Loffler, J.F., and Gehring, A.U. (2015)

837   Variable defect structures cause the magnetic low-temperature transition in natural monoclinic

838   pyrrhotite. Geophysical Journal International, 204, 961–967.

839   Kuipers, A.J.M., and Brabers, V.A.M. (1979) Electrical transport in magnetite near the Verwey

840   transition. Physical Review B, 20, 594–600.

841   Lapakko, K.A. (2015) Preoperational assessment of solute release from waste rock at proposed

842   mining operations. Applied Geochemistry, 57, 106–124.

843   Lashley, J.C., Hundley, M.F., Migliori, A., Sarrao, J.L., Pagliuso, P.G., Darling, T.W., Jaime,

844   M., Cooley, J.C., Hults, W.L., Morales, L., and others (2003) Critical examination of heat capacity

845   measurements made on a Quantum Design physical property measurement system. Cryogenics,

846   43, 369–378.

847   Levinson, L.M., and Treves, D. (1968) Mössbauer study of the magnetic structure of Fe7S8.

848   Journal of Physics and Chemistry of Solids.

849   Li, C.H. (1932) Magnetic Properties of Magnetite Crystals at Low Temperature. Physical

850   Review, 40, 1002–1012.

851   Li, G., Zhang, B., Baluyan, T., Rao, J., Wu, J., Novakova, A.A., Rudolf, P., Blake, G.R., de

852   Groot, R.A., and Palstra, T.T.M. (2016) Metal–Insulator Transition Induced by Spin Reorientation

853   in Fe7Se8 Grain Boundaries. Inorganic Chemistry, 55, 12912–12922.

854   Mikami, I., Hirone, T., Watanabe, H., Maeda, S., Adachi, K., and Yamada, M. (1959) On the

855   Magnetic Anisotropy of a Pyrrhotite Crystal. Journal of the Physical …, 14, 1568–1572.

856   Morimoto, N., Nakazawa, H., Nishigucmi, K., and Tokonami, M. (1970) Pyrrhotites:

857   Stoichiometric Compounds with Composition Fen--1Sn (n≥8). Science, 168, 964–966.

38

858   Muhlbauer, S., Honecker, D., Perigo, E., Bergner, F., Disch, S., Heinemann, A., Erokhin, S.,

859   Berkov, D., Leighton, C., Eskildsen, M., and others (2018) Magnetic Small-Angle Neutron

860   Scattering. Reviews of Modern Physics, submitted.

861   Muttoni, G. (1995) "Wasp-waisted" hysteresis loops from a pyrrhotite and magnetite-bearing

862   remagnetized Triassic limestone. Geophysical Research Letters, 22, 3167–3170.

863   Muxworthy, A.R., Bland, P.A., Davison, T.M., Moore, J., Collins, G.S., and Ciesla, F.J. (2017)

864   Evidence for an impact-induced magnetic fabric in Allende, and exogenous alternatives to the core

865   dynamo theory for Allende magnetization. Meteoritics & Planetary Science, 112.

866   Nakazawa, H., and Morimoto, N. (1970) Pyrrhotite Phase Relations below 320°C. Proceedings

867   of the Japan Academy, 46, 678–683.

868   O'Reilly, W., Hoffmann, V., Chouker, A.C., Soffel, H.C., and Menyeh, A. (2000) Magnetic

869   properties of synthetic analogues of pyrrhotite ore in the grain size range 1-24 μm. Geophysical

870   Journal International, 142, 669–683.

871   Oddou, J.L., Jeandey, C., Mattéi, J.-L., and Fillion, G. (1992) Mössbauer study of the low-

872   temperature transition in pyrrhotite. Journal of Magnetism and Magnetic Materials, 104-107,

873   1987–1988.

874   Pastor, J.M., Pérez-Landazábal, J.I., Gómez-Polo, C., Recarte, V., Larumbe, S., Santamarta,

875   R., Fernandes Silva, M., Gómez Pineda, E.A., Winkler Hechenleitner, A.A., and Lima, M.K.

876   (2012) Entropy change linked to the magnetic field induced Morin transition in Hematite

877   nanoparticles. Applied Physics Letters, 100, 063102.

878   Powell, A.V., Vaqueiro, P., Knight, K.S., and Chapon, L.C. (2004) Structure and magnetism

879   in synthetic pyrrhotite Fe_7S_8: A powder neutron-diffraction study. Physical Review B.

39

880   Quidelleur, X., Valet, J.-P., and Thouveny, N. (1992) Multicomponent magnetization in

881   paleomagnetic records of reversals from continental sediments in Bolivia. Earth and Planetary

882   Science Letters, 111, 23–39.

883   Rochette, P., Fillion, G., and Dekkers, M.J. (2011) Interpretation of Low-Temperature Data

884   Part IV: The Low-Temperature Magnetic Transition of Monoclinic Pyrrhotite. The IRM Quarterly,

885   21, 1–11.

886   Rochette, P., Fillion, G., Mattéi, J.-L., and Dekkers, M.J. (1990) Magnetic transition at 30–34

887   Kelvin in pyrrhotite: insight into a widespread occurrence of this mineral in rocks. Earth and

888   Planetary Science Letters, 98, 319–328.

889   Rochette, P., Lorand, J.P., Fillion, G., and Sautter, V. (2001) Pyrrhotite and the remanent

890   magnetization of SNC meteorites: a changing perspective on Martian magnetism. Earth and

891   Planetary Science Letters, 190, 1–12.

892   H. M. Rosenberg (1963) Low Temperature Solid State Physics, Oxford University Press, New

893   York,

894   Sato, K., Yamada, M., and Hirone, T. (1964) Megnetocrystalline Anisotropy of Pyrrhotite.

895   Journal of the Physical Scociety of Japan, 19, 1592–1595.

896   Schwarz, E.J., and Vaughan, D.J. (1972) Magnetic Phase Relations of Pyrrhotite. Journal of

897   geomagnetism and geoelectricity, 24, 441–458.

898   Sharp, W.E. (1966) Pyrrhotite: a Common Inclusion in South African Diamonds. Nature, 211,

899   402–403.

900   Shepherd, J.P., Koenitzer, J.W., Aragón, R., Spal ek, J., and Honig, J.M. (1991) Heat capacity

901   and entropy of nonstoichiometric magnetite $Fe_{3(1-\delta)}O_4$: The thermodynamic nature of the

902   Verwey transition. Physical Review B, 43, 8461–8471.

903   Shimada, K., Mizokawa, T., Mamiya, K., Saitoh, T., Fujimori, A., Ono, K., Kakizaki, A., Ishii,

904   T., Shirai, M., and Kamimura, T. (1998) Spin-integrated and spin-resolved photoemission study

905   of Fe chalcogenides. Physical Review B, 57, 8845–8853.

906   Shirai, M., Suzuki, N., and Motizuki, K. (1996) Electronic band structure and photoemission

907   spectra of Fe_7S_8. Journal of Electron Spectroscopy and Related Phenomena, 78, 95–98.

908   Tokonami, M., Nishiguchi, K., and Morimoto, N. (1972) Crystal structure of a monoclinic

909   pyrrhotite (Fe_7S_8). American Mineralogist, 57, 1066–1080.

910   van der Pauw, L.J. (1958) A method of measuring the resistivity and Hall coefficient on

911   lamellae of arbitrary shape, Philips Tech. Rev. **20**, 220

912   Volk, M.W.R., Gilder, S.A., and Feinberg, J.M. (2016) Low-temperature magnetic properties

913   of monoclinic pyrrhotite with particular relevance to the Besnus transition. Geophysical Journal

914   International, 207, 1783–1795.

915   Weiss, B.P., Maloof, A.C., Tailby, N., Ramezani, J., Fu, R.R., Hanus, V., Trail, D., Bruce

916   Watson, E., Harrison, T.M., Bowring, S.A., and others (2015) Pervasive remagnetization of detrital

917   zircon host rocks in the Jack Hills, Western Australia and implications for records of the early

918   geodynamo. Earth and Planetary Science Letters, 430, 115–128.

919   Wolfers, P., Fillion, G., Ouladdiaf, B., Ballou, R., and Rochette, P. (2011) The Pyrrhotite 32

920   K Magnetic Transition. Solid State Phenomena, 170, 174–179.

41

Preprint submitted to American Mineralogist February 15, 2018

921   Zhang, Kailong, Zhang, T., Liang, J., Zhu, Y., Lin, N., and Qian, Y. (2015) A potential

922   pyrrhotite (Fe 7 S 8) anode material for lithium storage. RSC Advances, 5, 14828–14831.

923   Zhang, Ke, Zheng, H., Wang, J., and Wang, R. (2008) Transmission electron microscopy on

924   iron monosulfide varieties from the Suizhou meteorite. Physics and Chemistry of Minerals, 35,

925   425–432.

926

Preprint submitted to American Mineralogist February 15, 2018

927
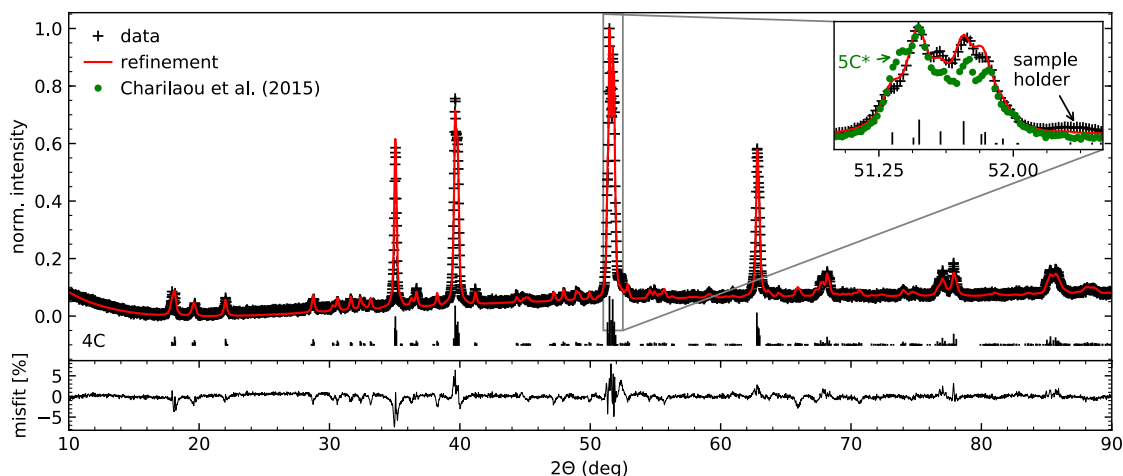
Figure 1: Powder X-ray diffraction (room temperature) of a sister specimen using Co radiation. The red line shows the fit obtained with Rietveld refinement. The inset shows an expanded view of the most prominent peak, in comparison with data from Charilaou et al. (2015) in green. The misfit is between the refinement and data.

43

Preprint submitted to American Mineralogist February 15, 2018

932
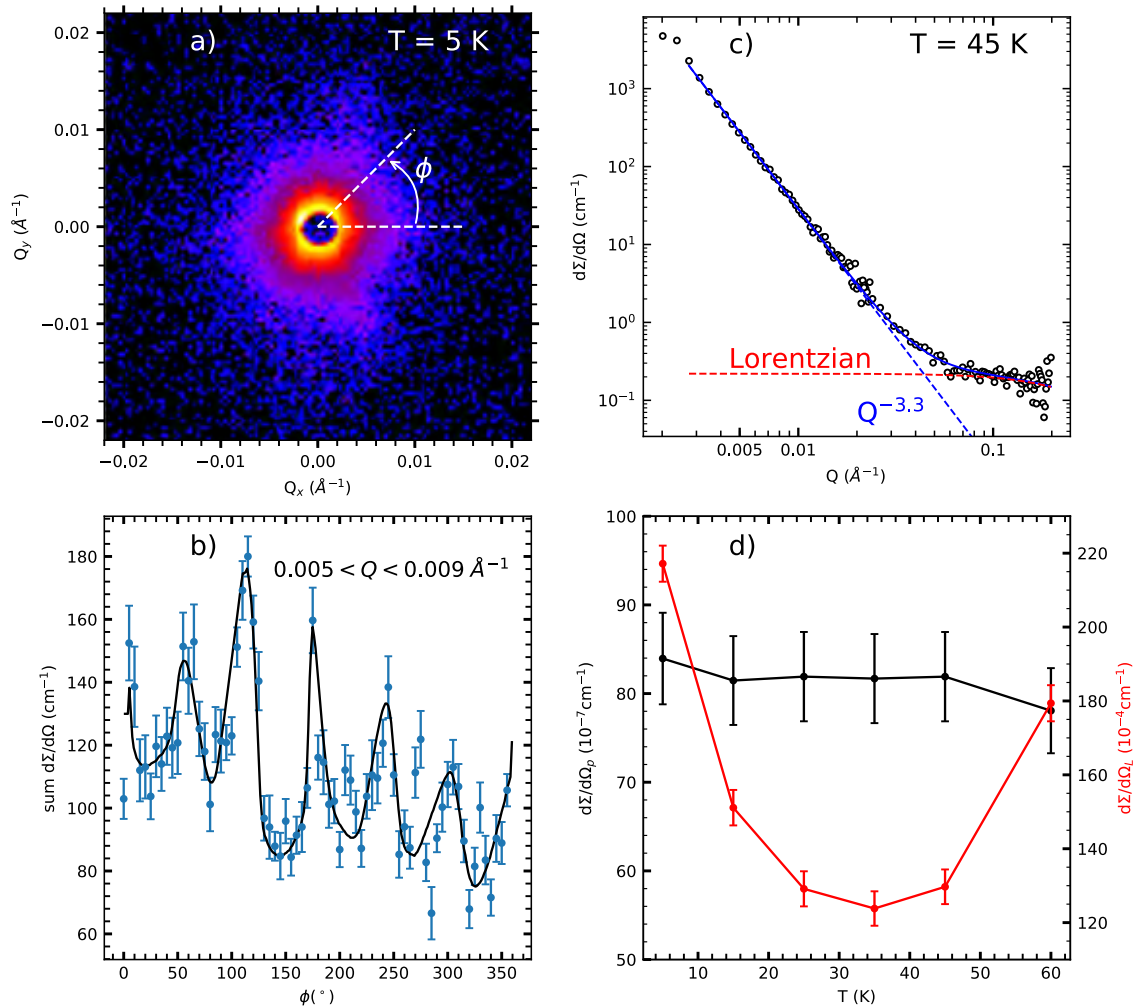
Figure 2: SANS results obtained with a 4C pyrrhotite crystal. a) The low Q 2D scattering
pattern (Q_x-Q_y map) obtained at 5 K (the brightness/color of each pixel indicates the differential
scattering cross-section). b) The sum of scattering cross-sections over the indicated low Q range
(0.005 Å^{-1} < Q < 0.009 Å^{-1}) as a function of the in-plane angle,ϕ, as defined in panel (a). These
data were averaged over all 6 temperatures probed (from 60 to 5 K), due to the absence of any
significant temperature dependence of the angular dependence. c) A representative (T = 45 K)
scattering cross-section ($d\Sigma/d\Omega$) vs. Q scan obtained by circular integration of the 2D scattering
patterns. The fit (solid blue line) is the sum of a Porod term (blue dashed line) and a Lorentzian
term (red dashed line), as discussed in the text. These two terms are defined by $d\Sigma/d\Omega$ =

44

Preprint submitted to American Mineralogist February 15, 2018

942    $(d\Sigma/d\Omega)_P/Q^n + (d\Sigma/d\Omega)_L /(Q^2 + \kappa^2)$, where "P" and "L" subscripts are for Porod and Lorentzian, n

943   is the generalized Porod exponent, and κ is defined in the text. d) The temperature (T) dependence

944   of the Porod (black) and Lorentzian (red) cross-sections, .

945

Preprint submitted to American Mineralogist February 15, 2018

946
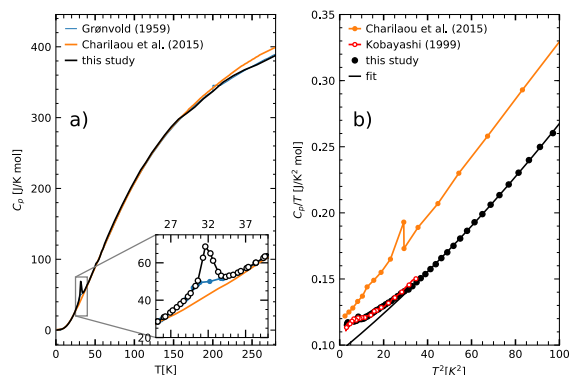
947

948   **Figure 3:** Heat capacity measurements obtained in this study along with those from previously

949   published studies. (a) C_P as a function of temperature (T), with the inset focusing on the Besnus

950   transition at 32 K. The solid lines are simple linear segments connecting data points. (b) C_P/T as a

951   function of T^2 at low temperature. The solid black line is a fit to the data as described in the text.

952

46

953

954
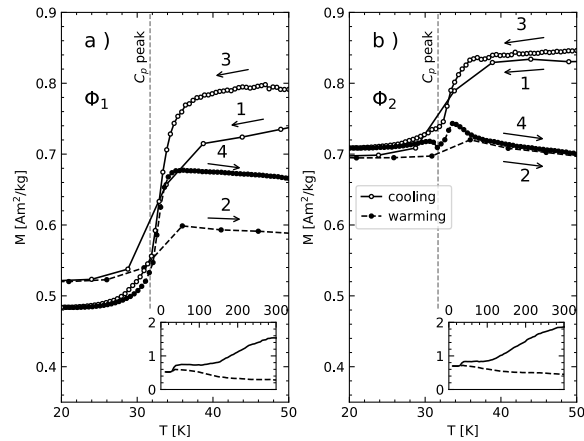
Figure 4: Zero field low-temperature cycling of a room temperature SIRM moment acquired in a 2.5 T field in the basal (a-b) plane. a) and b) show different orientations of the single crystal. The experiment was repeated twice for each orientation, where the first experiment was measured using a larger temperature interval (every 5 K) than the second experiment (every 0.5 K). The magnetization in the second experiment is usually higher than in the first, suggesting a slight hardening after the first thermal cycling. Arrows show cooling or warming, numbers indicate the measurement sequence. Dashed lines denote the temperature of the heat capacity peak. Insets in both (a) and (b) are SIRM moments over the entire temperature range measured, with solid lines being the cooling paths and dashed lines warming.

47
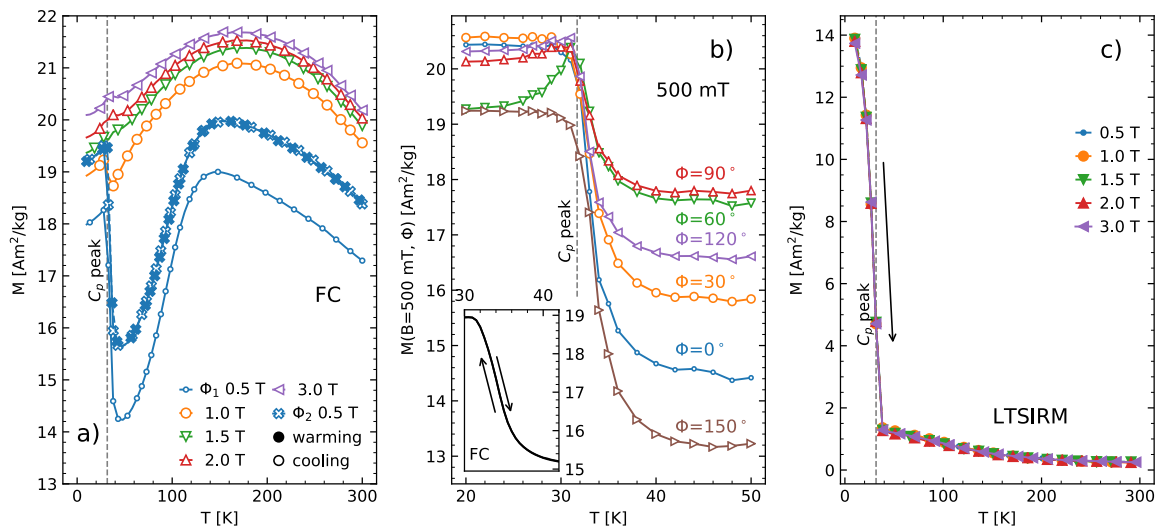
964

965   **Figure 5:** Field cooling (FC) experiments in different fields a). FC in 500 mT was measured

966   along two arbitrary, perpendicular directions in the basal plane (Φ_1, Φ_2). Crosses mark direction Φ_2

967   on cooling and warming (filled marker). b) shows M(B = 500 mT, T, Φ) determined from

968   hysteresis loops (see text) at selected orientations within the basal plane of an oriented single

969   crystal of Fe_7S_8. Inset in b) demonstrates the lack of hysteresis of a high-resolution (0.5 K) FC

970   measurement (see a)) in a 500 mT field (Φ_1) on warming and cooling. c) shows warming of a low-

971   temperature SIRM acquired by cooling in field (a) to 10 K.

972

48

973
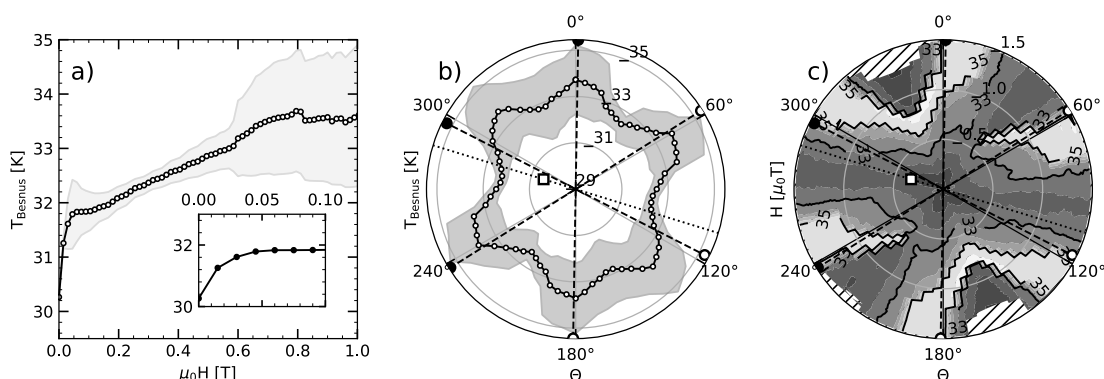
974 **Figure 6:** Transition temperature calculated from the maximum of dM/dT of the positive

975 ascending branch of the hysteresis loop for all orientations and fields. a) Average transition

976 temperature with one standard deviation (shaded region) for all orientations as a function of

977 magnetic field. The inset shows a zoomed-in view of the first 100 mT b) Directional dependence

978 of the mean transition temperature over all applied fields. A data point's distance from the center

979 of the plot corresponds to the T_{Bes} for that orientation and varies between 29 and 35K. The shaded

980 region shows 1σ uncertainty. c) Contour plot for all fields (radius) and orientation (angle), dark =

981 low, light = high transition temperature. Hashed regions show the area where T_{Bes} could not be

982 calculated. Solid lines in b) and c) show the crystallographic axis as determined by EBSD. The

983 dashed line is the projection of the c-axis onto the plane.

984

Preprint submitted to American Mineralogist February 15, 2018
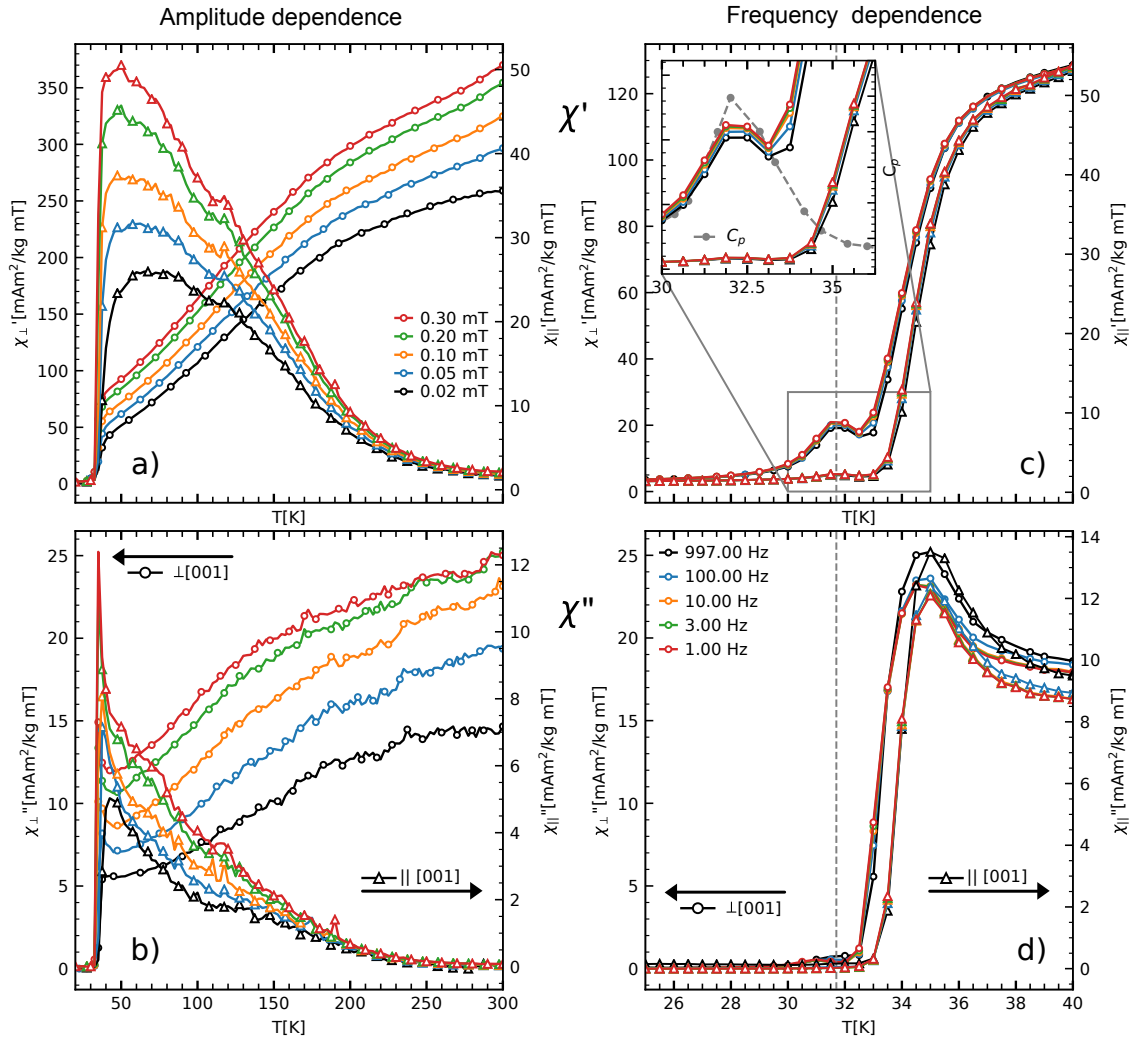
Figure 7: Mass-normalized in-phase (χ') and out-of-phase (χ'') susceptibility as a function of temperature in different field amplitudes (a, b) (frequency = 100 Hz, marker every 4th measurement) and frequencies (c, d) (amplitude = 0.30 mT). Circles show measurements within the basal plane ($\chi_\perp$) of the crystal, while triangles show measurements done along the crystallographic c-axis ($\chi_{||}$, secondary y-axis). Dashed vertical lines show the maximum from the heat capacity measurement. Inset shows a zoom into the secondary peak overlaid with specific heat data (see. fig. 2) in arb. units. The background in specific heat was removed by polynomial interpolation.

50

994
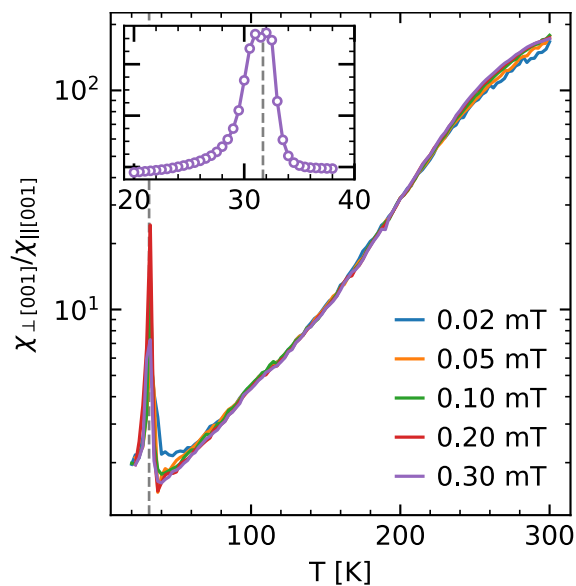
Figure 8: Ratios of in-plane over out-of-plane susceptibilities ($\chi_\perp/\chi_\parallel$) as a function of temperature for different field amplitudes. The inset shows the ratio determined from high-resolution AC susceptibility data (100 Hz, 0.3 mT). The dashed line shows the transition temperature determined from specific heat.

51

999
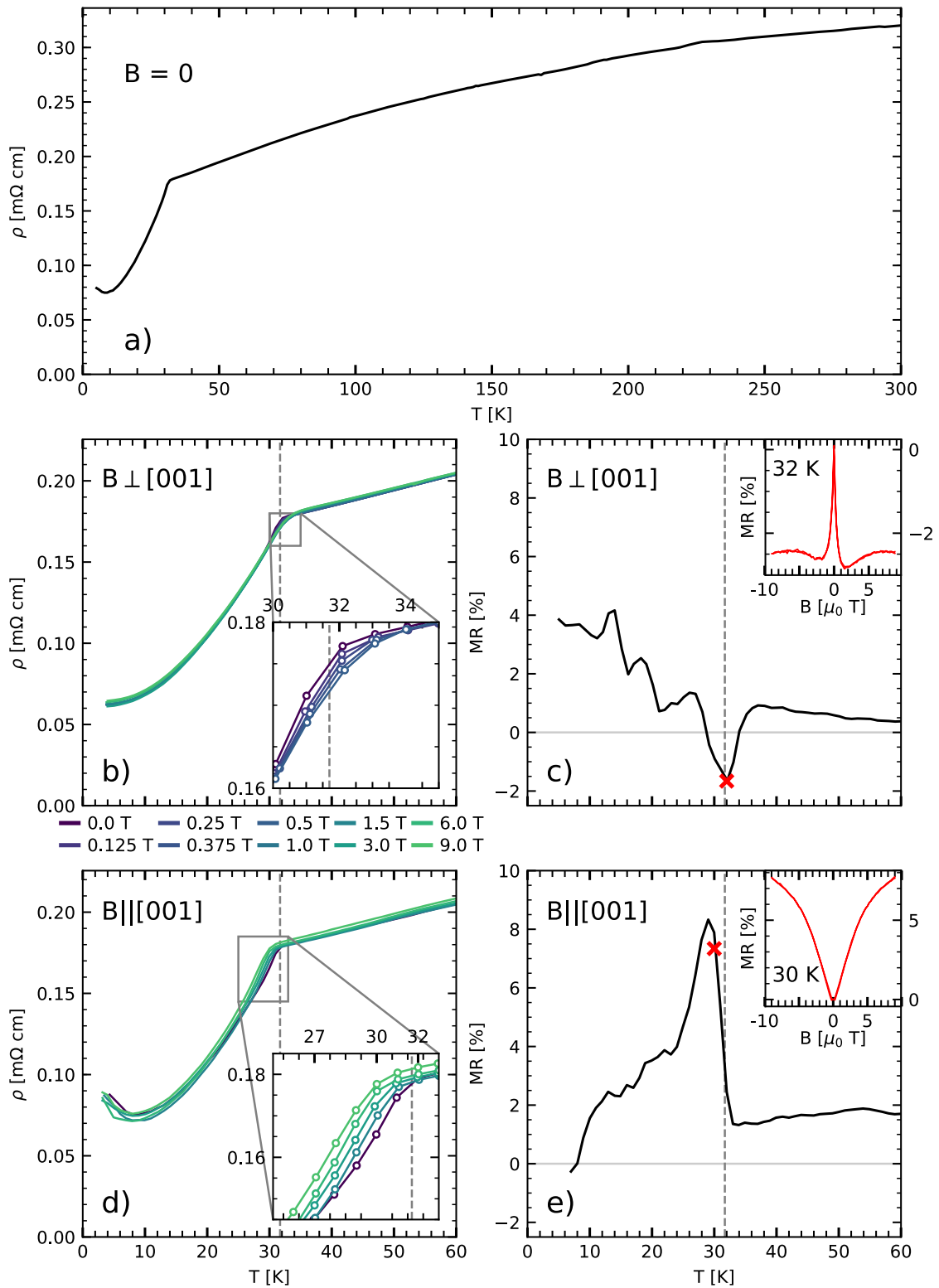
Figure 9: 4C pyrrhotite single crystal electrical resistivity measured via the van der Pauw

method as a function of temperature and magnetic field. (a) a-b plane resistivity (ρ) as a function

52

1002   of temperature (T) upon warming from 4 K to 300 K in zero field (B). (b-d) show expanded views

1003   of transport and magnetotransport properties in the T_{Bes} region. (b) ρ vs. T as a function of B (from

1004   0 – 0.5 T) applied in the basal plane. (c) Corresponding magnetoresistance (MR) as a function of

1005   T at 9 T. The inset shows the B dependence of the MR at 32 K. (d) ρ vs. T as a function of B (from

1006   0 - 9 T) applied along [001]. (e) Corresponding MR as a function of T at 9 T. The inset shows the

1007   B dependence of the MR at 30 K. Red crosses in (c) and (e) mark the measurement temperature

1008   for the MR(B) traces shown in the insets.

1009

Preprint submitted to American Mineralogist February 15, 2018
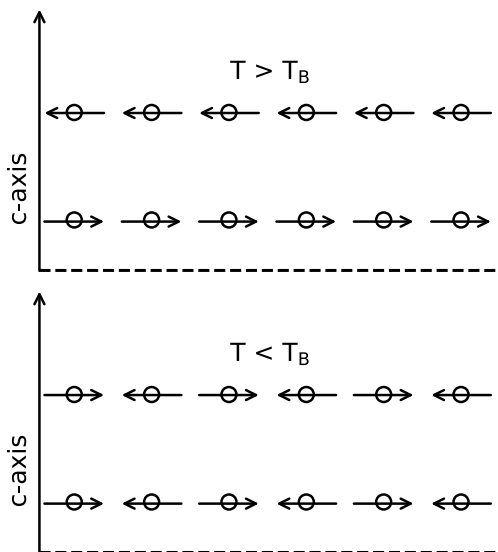
1010

1011   **Figure 10:** Schematic representation of exchange inversion. Arrows indicate the spins of the

1012   atoms.

1013

Preprint submitted to American Mineralogist February 15, 2018

1014 **Table 1**: Mean saturation magnetization ($M_s(\theta_1, \theta_2)$) determined from in-field cooling in a 3 T

1015 field and saturation remanence (M_{rs}) at 10 (LTSIRM) and 300 K (RTSIRM).

	M_{rs} [Am²/kg]	M_s [Am²/kg]	M_{rs}/M_s
10 K	13.85	20.09	0.69
300 K	1.67	20.19	0.08

1016

1017

Preprint submitted to American Mineralogist February 15, 2018

1018   **Table 2:** Amplitude dependence of susceptibility above (300 K) and below (20 K) T_{Bes}.

1019   Absolute values of the susceptibility are given in mAm^{2}kg^{-1}mT^{-1}

Amplitude in mT	0.2	0.5	1.0	2.0	3.0
$\chi_{\parallel}$ (300 K)	1.55	1.68	1.82	2.04	2.15
$\chi_{\parallel}$ (20 K)	0.97	0.97	0.95	0.96	0.96
$\chi_{\parallel}$ (20 K / 300 K) [%]	62.26	57.72	52.09	47.22	44.74
$\chi_{\perp}$ (300 K)	258.96	296.64	324.94	354.51	370.13
$\chi_{\perp}$ (20 K)	1.84	1.82	1.84	1.83	1.83
$\chi_{\perp}$ (20 K / 300 K) [%]	0.71	0.61	0.57	0.52	0.50
$\chi_{\perp}/\chi_{\parallel}$ (300 K)	166.86	176.60	178.43	174.15	172.55
$\chi_{\perp}/\chi_{\parallel}$ (20 K)	1.91	1.87	1.94	1.91	1.91

1020

1021